BACKGROUNDS TO SENSITIVE EXPERIMENTS UNDERGROUND

Joseph A. Formaggio[1] and C.J. Martoff[2]

[1]*Center for Experimental Nuclear Physics and Astrophysics, University of Washington, Seattle, Washington 98195;* [2]*Department of Physics, Temple University, Philadelphia, Pennsylvania 19122; email: josephf@u.washington.edu; cmartoff@ba325.scitech.temple.edu*

Key Words underground science, atmospheric neutrinos, proton decay, solar neutrinos, double beta decay, dark matter, backgrounds, spallation, cosmogenesis

Abstract We summarize residual background sources encountered in experiments conducted deep underground. Physical mechanisms of production and methods of estimation for the dominant sources are considered, and comparisons of the calculations with underground measurements are discussed. Principal background sources discussed include primary interactions of cosmic rays, mechanisms of neutron production by cosmic rays and low energy backgrounds from neutrons, primordial and anthropogenic radionuclides, and secondary radioactivity from spallation.

CONTENTS

1 INTRODUCTION

For the past 40 years, sensitive experiments performed deep underground have revealed a wealth of knowledge about some of the most elusive phenomena of nature. Only the environment beneath the Earth's surface provides the conditions necessary for experiments dealing with these rare or exotic phenomena. Protected from cosmic rays, which can lead to an overwhelming rate of interactions, underground experiments have revealed detailed and unanticipated information about phenomena ranging from the micro-world of neutrinos to some of the most energetic events in the universe (supernovae). Unlocking the profound mystery of galactic dark matter by its direct detection can also only be pursued underground.

The dominant background sources remaining in underground environments differ in character from those normally found on the surface. Special techniques have been developed to shield out, discriminate against, or accurately measure the background present in these experiments.

This paper reviews the sources of background that are important in underground environments. A review by Heusser on low-radioactivity background techniques addressed related issues (1). This paper is intended to complement that review.

2 SENSITIVE UNDERGROUND EXPERIMENTS

Before describing in detail the types of backgrounds present in underground experiments, it is useful to discuss the different kinds of experiments performed underground. A thorough analysis of all types of underground experiments is beyond the scope of the paper. Instead, we briefly overview a select subset of these experiments, mainly proton decay, dark matter, solar neutrino, and neutrinoless double beta decay experiments.

2.1 Atmospheric Neutrino and Proton Decay Experiments

The use of underground laboratories for the study of cosmic rays was already established by the 1960s. Among the first of these experiments were direct searches for atmospheric neutrinos. Two separate groups—Reines and colleagues using the East Rand Proprietary Mine, near Johannesburg, South Africa (2) and Menon and colleagues using the Kolar Gold Mines in India (3)—independently measured the rate of atmospheric neutrinos by looking at neutrino-induced muons coming horizontally through the detector. These groups operated at underground depths of 8900 and 7500 meter water equivalents (mwe)[1] respectively, which to this day are still truly remarkable. These two experiments provided the first observations of neutrinos produced in the atmosphere. The results also established underground detectors as a sound method to study phenomena that otherwise would be overwhelmed by much more intense cosmic radiation at the Earth's surface.

Since then, the study of atmospheric neutrinos underground has grown into an active and important field of research. The progenitors of today's atmospheric neutrino experiments were the Irvine Michigan Brookhaven Experiment (IMB), located in the Morton salt mine near Cleveland, Ohio (4); and the Kamioka experiment, located in the Mozumi zinc mine in Japan (5). Both experiments were originally designed to search for proton decay using massive water Cherenkov detectors. These reconstruct the tracks of muons with energy above several hundred MeV. Other experiments contemporary to the first water Cherenkov detectors, such as Fréjus (6) and NUSEX (7), both located in France, made similar measurements using iron calorimetry. The results from these experiments prompted the current generation of atmospheric neutrino experiments to be proposed and built. These include the MACRO and Soudan 2 experiments (8, 9), both iron tracking calorimeters, and the 50-ton upgrade to Kamiokande, Super-Kamiokande (10).

Each of the aforementioned detectors can serve both as atmospheric neutrino and proton decay experiments. Most extensions to the standard model predict a finite lifetime for the proton (11). Decay mechanisms depend on the particulars of the given model, though decays such as $p \rightarrow e^+\pi^0$ and $p \rightarrow K^+\nu$ are typically predicted to be dominant. Proton decay results from all the above experiments

---

[1] Throughout the paper, we use meter water equivalents (mwe) to denote depth in units of 100 g/cm^2. Unless otherwise stated, we assume standard rock ($\langle Z \rangle = 11$; $\langle A \rangle = 22$; $\rho = 2.65$ g/cm^3).

have so far been negative, which excludes a large number of grand unified theory (GUT) models (11).

While setting limits on proton decay, these experiments also provided the first evidence that the ν_μ/ν_e ratio for atmospheric neutrinos was considerably smaller than that predicted by theoretical calculations. Such an observation would be most simply explained by the phenomenon of neutrino oscillations, whereby a ν_μ oscillates into a ν_τ. Final confirmation came from the Super-Kamiokande experiment, in which the ν_μ and ν_e fluxes were studied as a function of zenith angle (12). This result, along with measurements made with solar neutrinos (see below), helped firmly establish the phenomenon of neutrino oscillations. The proposed next-generation proton decay and atmospheric neutrino detectors, such as AQUA-RICH (13), UNO (14), and Hyper-Kamiokande (15), build upon the proven success of Super-Kamiokande and its contemporaries.

2.1.1 BACKGROUNDS IN PROTON DECAY EXPERIMENTS Nucleon decay modes sought in underground searches release several hundred MeV of visible energy in the form of a small number of particles. Such decays have a number of highly specific signatures, so the background requirements for present and future experiments of this type are relatively modest compared with those of other underground experiments. The main background is from atmospheric neutrinos, whose energy and interaction topology can mimic that of proton decay. Neither depth nor shielding can reduce this background, which must be removed using appropriate event selection criteria (4). In addition to atmospheric neutrinos, backgrounds may arise from fast neutrons produced by high-energy cosmic rays. The neutron spectrum produced by cosmic ray muons deep underground can extend up to several GeV. Shielding against such energetic neutrons is essentially futile since the required very thick shields (hundreds of g/cm^2) will simply serve as an additional neutron production target. Attenuating the cosmic ray muons by operating deeper underground is the most effective way to reduce this background. Finally, additional background can come from the activation of certain isotopes that mimic specific signatures for proton decay. For example, certain searches for proton decay via $p \rightarrow K^+\nu$ within a ^{16}O nucleus will leave a ^{15}N daughter, usually in an excited state. This mode of proton decay has been sought by tagging the kaon decay $K^+ \rightarrow \mu^+\nu_\mu$ in coincidence with the de-excitation gamma ray(s) from ^{15}N (16). A high gamma accidental rate due to inadequate shielding or radioactive contamination can pose problems for such a measurement.

2.2 Solar Neutrino Experiments

Direct study of the energy-producing nuclear reactions occurring in the sun's core began with the pioneering work of Ray Davis, Jr. (17, 18). This groundbreaking radiochemical experiment was the first to successfully use extremely rare neutrino interactions to probe the sun. Moving such an "industrial scale" experiment underground to provide the essential shielding against cosmic rays still serves as a model for current and proposed rare-event experiments.

The original experiment designed by Davis, located 1500 m underground in the Homestake mine, used 610 tons of perchloroethylene (C_2Cl_4) to search for the neutrino induced reaction $^{37}\mathrm{Cl}(\nu_e, e^-)^{37}\mathrm{Ar}$, shorthand for $\nu_e +^{37}\mathrm{Cl} \rightarrow e^- +^{71}\mathrm{Ge}$. In this reaction, neutrinos above the 814 keV threshold can increase the atomic number of the ^{37}Cl by one unit. The results showed only one third of the neutrino flux predicted by the standard solar model (19).

This “solar neutrino problem” persisted for decades, finally being confirmed by a number of subsequent experiments—each taking advantage of the reduction of backgrounds that resulted from siting the experiment underground. Later radiochemical experiments such as SAGE in the Baskan Neutrino Observatory (20), GALLEX (21), and GNO (22) in Mont Blanc, made use of the neutrino capture process ^{71}Ga (ν_e, e^-) ^{71}Ge (threshold 233 keV) to measure the dominant low-energy component of the solar neutrino flux.

Real-time experiments such as Kamiokande (5) and Super-Kamiokande (10) have made use of the elastic scattering process $\nu_x + e^- \rightarrow \nu_x + e^-$ to measure the high-energy ^{8}B component of the solar neutrino flux. The threshold for recoil electron detection in these experiments was about 8 MeV. In all cases, only between 1/3 and 1/2 of the expected flux was measured, depending on the neutrino energy.

The shortfall was finally explained by the Sudbury Neutrino Observatory (SNO), located in Sudbury Canada. The SNO experiment measured both the flavor-independent neutral-current reaction $\nu_x + d \rightarrow \nu_x + p + n$ i and the charged-current, ν_e-only reaction $\nu_e + d \rightarrow e^- + p + p$ on deuterium in a D_2O target (23–25). From these data, the total active flux of neutrinos was found to be consistent with full standard-solar-model strength, with the shortfall in electron-type neutrinos explained by the phenomenon of neutrino oscillations (26).

The future of solar neutrino experiments is in refined measurements of the low-energy portion of the solar neutrino spectrum. A graph of the predicted solar neutrino flux (without oscillations) is shown in Figure 1. The energy range below the ^{8}B flux, and in particular the dominant *pp* energy spectrum, yields more information on the neutrino mixing parameters and provides precise tests of the

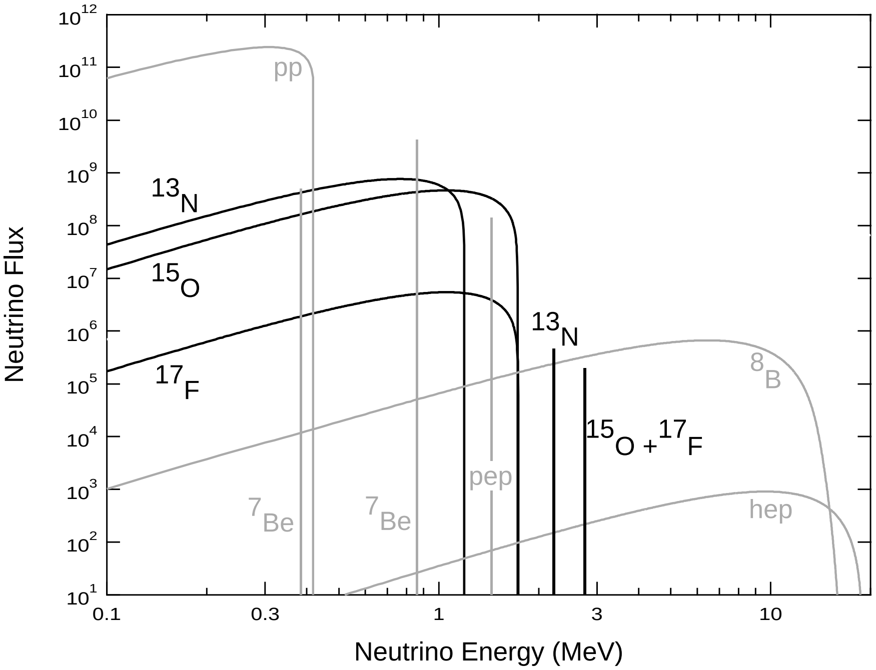

Figure 1: Solar neutrino flux at 1 A.U., including electron capture in the CNO cycle. The *pp* chain is shown in grey and the CNO cycle is shown in black. Line fluxes are in cm^{-2} s^{-1} and continuum fluxes are in cm^{-2} s^{-1} MeV^{-1}. Flux values taken from Reference (27) and Bahcall's website (www.sns.ias.edu/∼jnb/).

solar energy production mechanism. Several new solar neutrino experiments have been proposed, a few of which are mentioned here. Some proposed experiments, such as CLEAN (liquid neon) (28), HERON (superfluid liquid helium) (29), and XMASS (enriched liquid Xenon) (30), use the elastic scattering on electrons to measure the *pp* and ^{7}Be flux from the sun. Because the cross section is known with great precision ($\sim 1\%$), this reaction allows the low-energy neutrino spectrum to be extracted very accurately. Similarly, BOREXINO (liquid scintillator; currently under construction) (31) will allow measurement of the ^{7}Be and CNO neutrinos from the sun with high precision. Finally, proposed experiments such

Table 1: Current and projected experimental sensitivities for various components of the solar neutrino flux. Theoretical uncertainties of neutrino flux sources are also shown (35)

	pp	CNO	^{7}Be	^{8}B
Current uncertainty	18%	100%	35%	8%
Proposed experiments	12%	100%	8%	6%
Next-generation experiments	1–3%	2–5%	5–10%	2–5%
Theoretical uncertainty	1%	$\sim$ 40%	12%	20%

as LENS (32) and MOON (33) use the charged-current neutrino reactions ^{115}In $(\nu_e, e^-)^{115}$Sn and ^{100}Mo $(\nu_e, e^-)^{100}$Tc, respectively to measure the neutrino flux from the *pp* chain. Table 1 shows estimates of the expected precision from these near-term and long-term future experiments (34).

2.2.1 BACKGROUNDS IN SOLAR NEUTRINO EXPERIMENTS As the technology of low-energy neutrino experiments is pushed farther to achieve the required precision, the background requirements become more and more stringent. Background requirements differ depending on the technique and sensitivity of the experiment. SNO, for example, gets its neutrino-flavor-independent sensitivity from the neutral-current disintegration of deuterium [^{2}H$(\nu_x, \nu_x')np)$], producing a single-neutron event signature. Background photons above 2.2 MeV produced in the uranium and thorium decay chains could photodisintegrate deuterium, resulting in a background nearly indistinguishable from the neutral-current signal. CLEAN and HERON are also sensitive to high-energy external gammas produced from impurities in detector material. Experiments such as BOREXINO, which depend on measuring low-energy events in scintillator, are sensitive to radioactive decays of cosmogenic isotopes such as ^{3}H and ^{14}C, as well as ^{40}Ar, ^{85}Kr, and radon. All solar neutrino experiments require very clean instrumentation, low natural background radioactivity, and sufficient overburden to reduce cosmic ray activity. As shown in the following sections, such requirements are common to other types of experiments as well.

2.3 Double Beta Decay Experiments

The search for neutrinoless double beta decay ($\beta\beta0\nu$) has a long history (36). Interest has recently been stimulated by confirmation of neutrino oscillations in both atmospheric and solar neutrino experiments, and the realization that the mass limit implied by the oscillation results is within the grasp of current and next-generation $\beta\beta0\nu$ experiments. Recent reviews on the subject of neutrinoless double beta decay exist (37, 38), so we provide only a brief review of the topic focused on the issues pertinent to backgrounds.

Double beta decay is an extremely rare process that connects nuclei with the same mass number and nuclear charge differing by two units. Only a few pairs of isobars exist for which the process is exoergic. So far, only the lepton-number-conserving two-neutrino mode [$\beta\beta(2\nu)$] has been experimentally observed:

$$(Z, A) \rightarrow (Z+2, A) + e^{-} + e^{-} + \bar{\nu_e} + \bar{\nu_e}. \tag{1}$$

By contrast, in the neutrinoless double beta decay [$\beta\beta(0\nu)$], no neutrinos are present in the final state:

$$(Z, A) \rightarrow (Z+2, A) + e^{-} + e^{-}. \tag{2}$$

The latter process violates lepton number conservation and can only occur under two conditions: (*a*) the neutrino is a Majorana particle (particle and antiparticle states are identical) and (*b*) the neutrino has nonzero mass. The $\beta\beta(2\nu)$ and $\beta\beta(0\nu)$ decays are easily distinguishable from one another because in the former the energy is shared among four light particles (two of them unobservable), giving a continuum spectrum of deposited energy. In the latter all the energy of the decay is carried by the two electrons giving a monoenergetic peak of deposited energy. Therefore, a highly sensitive neutrinoless double beta decay experiment of the conventional nuclear-spectroscopic type requires the best possible energy resolution, and the lowest possible background at energies near the $\beta\beta(0\nu)$ Q-value.

In a real-time counting experiment with a live target/detector containing N $\beta\beta$-active nuclei and a counting time t, the experimental upper limit on the $\beta\beta$ decay rate scales as $\langle m_\nu \rangle \sim 1/\sqrt{Nt}$ for background-free experiments and $< m >\sim 1/(Nt)^{1/4}$ for situations when the background increases linearly with Nt. These statistical results, which apply to all counting experiments, show the qualitative change in the rate of sensitivity improvement once background begins to appear. Complete suppression of background to a level below the counting rate corresponding to the desired limit is a great advantage. A more advanced strategy is proposed for the EXO experiment(39), using a unique combination of real-time counting and a laser-spectroscopic "radiochemical" method to identify the final-state atoms one at a time. Such next-generation strategies are intended to allow limits on the neutrino Majorana mass to be pushed down by more than an order of magnitude, mainly by eliminating more background using the event signature. However, the requirements on the gross background rate will still be extremely stringent.

2.3.1 Backgrounds in ($\beta\beta0\nu$) Experiments In conventional nuclear-spectroscopic experiments, any activity that deposits energy near or above the Q-value of the reaction is a source of background. Of particular concern is contamination from natural radioactivity, such as long-lived uranium and thorium isotopes. For example, ^{214}Bi (from the uranium decay chain) and ^{208}Tl (from the thorium decay chain) emit relatively high-energy photons (2.45 MeV and 2.61 MeV, respectively). Because uranium and thorium are found in surrounding rock environments, and trace amounts exist in construction materials, experiments and their surroundings must be made as free as possible from such contaminants. A troublesome route of contamination is radon gas (^{222}Rn and ^{220}Rn) which diffuses into the air and produces background if it enters a detector's sensitive region.

Other backgrounds affecting sensitive double beta decay experiments are from cosmic rays. Secondary radioactivity is unavoidably produced in the detector and the shielding itself whenever they are subjected to the surface cosmic ray flux. This often proves very difficult to reduce or eliminate. Fast neutrons are also produced by the cosmic rays, and high-energy photons may come from the cosmic ray cascades themselves or as secondaries from thermal neutron capture. Minimizing time spent on the surface and maximizing the depth of the underground lab are important in determining the background levels of a double beta decay experiment.

2.4 Dark Matter Experiments

2.4.1 Direct Detection Experiments and Their History Since the earliest astrophysical measurements of galaxy clusters during the 1930s (40), observations have strongly suggested that much of the gravitating mass in large

Table 2: Summary of current and proposed double beta decay experiments. Right arrow (→) indicates the projected sensitivity of the experiment.

Experiment	Isotope	Technique	Mass (kg)	Enriched	$Q_{\beta\beta}$ (MeV)	$< m_\nu >$
Heidelberg	^{76}Ge	Ge crystals	9.9	86%	2.04	< 0.40
IGEX	^{76}Ge	Ge crystals	9	86%	2.04	< 0.44
UCI	^{82}Se	TPC foils	0.014	97%	2.99	< 7.7
ELEGANT	^{100}Mo	Drift chambers	0.20	94.5%	3.03	< 2.7
Kiev	^{116}Cd	$CdWO_4$ crystals	0.09	83%	2.8	< 3.3
Missouri	^{128}Te	Geochemical	Te Ore	No	0.87	< 1.5
Milano	^{130}Te	Cryogenic TeO_2	2.3	No	2.53	< 2.6
UCI	^{150}Nd	TPC foils	0.015	91%	3.37	< 7.1
NEMO3	^{82}Se,^{100}Mo, ^{116}Cd,^{150}Nd	Drift chambers	Varies	Yes	Varies	→ 0.1
CUORICINO	^{130}Te	Cryogenic TeO_2	2.3	No	2.53	→ 0.1
GENIUS	^{76}Ge	Ge crystals	1000	Yes	2.04	→ 0.01
MAJORANA	^{76}Ge	Ge crystals	500	Yes	2.04	→ 0.02
CAMEO	^{82}Se,^{100}Mo, ^{116}Cd	BOREXINO CTF	1 each	Yes	Varies	→ 1
MOON	^{100}Mo	Scintillator foils	3400	No	3.03	→ 0.02
CUORE	^{130}Te	Cryogenic TeO_2	210	No	2.53	→ 0.02
EXO	^{136}Xe	TPC	10,000	Yes	2.47	→ 0.01
DBCA-II	^{150}Nd	Drift chambers	18	Yes	3.37	→ 0.05

structures is invisible, i.e., it does not emit or absorb electromagnetic radiation (41). Orbital velocities in large systems are systematically larger than they should be in the gravitational potential well of their visible mass.

The idea that the invisible or "dark" matter could be sought in low-background counting experiments arose in the 1970s as a result of several converging lines of evidence. Big bang nucleosynthesis calculations became widely accepted, and these indicated that most of the dark matter had to be non-baryonic (42). Lee & Weinberg (43) originated a general argument—which was soon extended (44)—showing that if any member of a broad class of stable, weakly interacting massive particles (WIMPs) existed in nature, they would remain today as a "big bang relic" population with approximately the mass density of the astrophysical dark matter. Supersymmetric particle theories provided a generic identity for such a WIMP dark matter particle: the lightest super-partner (LSP) or neutralino (45). It was soon recognized that WIMP dark matter was in principle detectable by recoil atoms from its elastic scattering in low-background detectors (46, 47). The first experimental attempts to detect WIMPs by elastic scattering used low-energy data from low-background semiconductor detectors (48,49). Seminal treatises on the general detection problem (50,51) appeared at about this time, which still provide a useful guide to the subject.

Direct detection of WIMP dark matter is now a mini-industry, with many experiments using a wide variety of techniques either operating or planned. Detection of a signal has been reported by one group for several years (52), but at the time of writing, this result remains to be confirmed. An up-to-date online database of results is maintained by Gaitskell and Mandic (53).

Table 3 lists dark matter search experiments currently operating underground.

A list including all experiments proposed or under construction would be very long and is beyond the scope of this review.

2.4.2 DISCRIMINATION—REDUCTION OF "ACCEPTED BACKGROUND"

Every experiment in Table 3 measures the energy of individual events, at least to some degree. This is the simplest example of what has come to be called discrimination: reduction of the "accepted background" by measurement of event characteristic(s) that allow some events to be a priori rejected or assigned a very low probability of being WIMP interaction candidates. Discrimination by energy relies on the fact that events above ∼200 keV are very unlikely in nearly any WIMP model and thus need not be considered as WIMP candidates in standard analyses. Of course, such a strategy has its limitations. Physical background radiation above 200 keV will also usually produce energy depositions less than the full energy peak (e.g., Compton tails). Low absolute background levels remain essential for direct-detection WIMP searches even with effective discrimination.

First-generation WIMP searches (48, 49) essentially measured only the energy of events and therefore required extremely low total background. This strategy was exemplified by the HDMS experiment and had a long history of yielding the best available upper limits on WIMP interaction rates (54, 55). This philosophy is still being actively pursued (56). A detector measuring only energy does have the advantage of simplicity and relies only on the best-understood aspects of detector response. Some experiments of this type [particularly CRESST I (57)] also gained sensitivity by having quite low energy thresholds. However, in an energy-only measurement any event depositing energy in the allowed region must be accepted. This requires shielding from external radiation and reductions in internal radioactivity down to levels that are extraordinary even by the standards

Table 3: Selected direct dark matter search experiments currently in operation. Detection techniques include scintillation (Sc), ionization (Ion), time-projection chamber (TPC), or bolometry (Bol). Published limits are shown for either spin-independent (SI) or spin-dependent (SD) targets. Asterisk (*) denotes signal rather than limit.

Experiment	Detection technique	Location	Target	Limit (pb/Nucleon)
ANAIS	Sc	Canfranc	NaI (10.7) kg	$<4\times 10^{-4} SI$
CDMS	Bol, Ion	Soudan	Ge (495 g) + Si (100g)	$<4\times10^{-6}$ SI
CRESST	Bol, Sc	LNGS	Al_2O_3 (262 g)	< 0.1 SD
DAMA	Sc	LNGS	NaI (100 kg)	10^{-5}–10^{-6}SI *
DRIFT	NI-TPC	Boulby	CS_2 (160 g)	–
EDELWEISS I	Bol, Ion	Modane	Ge (960 g)	$<2\times10^{-6}$ SI
ELEGANTS	Sc	Oto-Cosmo	NaI (∼365 kg)	$<2\times10^{-4}$ SI
HDMS	Ion	LNGS	^{73}Ge (202 g)	$\sim 1\times10^{-5}$ SI
IGEX	Ion	Baksan, Canfranc	^{76}Ge (6 kg)	8×10^{5} SI
MIBETA	Bol	LNGS	TeO_2 (340 g)	10^{-4} SI
Modane NaI	Sc	Modane	NaI (10 kg)	1.3×10^{-4} SI
NaIAD	Sc	Boulby	NaI (46 kg)	2×10^{-5} SI
PICASSO	SDD	Sudbury	C_nF_{2n} (1 g)	1.5×10^{1} SD
ROSEBUD	Bol, Sc	Canfranc	$CaWO_4$; (54 g)	10^{-2} SI
Tokyo LiF	Bol	Kamioka	LiF (168 g)	20 SD
UKDMC-NaI	Sc	Boulby	NaI (6 kg)	8×10^{-5} SI 1.5 S

of the field.

All the “dual detection modality” experiments in Table 3 use some form of discrimination in addition to energy measurement. The principal strategy is to find a way to distinguish the nuclear recoil events expected for the WIMP signal from other events produced by radioactive background. Background sources other than neutron scatters (i.e., beta decays and x-ray and gamma-ray interactions) will actually deposit their energy in the form of low-energy electrons, which have much lower dE/dx than recoil nuclei depositing the same total energy. In condensed-matter targets, WIMP-candidate track lengths are $\sim 0.1\ \mu$m, too small to allow for direct measurement of dE/dx. The tracks can be made longer and directly measured using a low-density gas detector such as DRIFT (58, 59). A recoil-tracking experiment like DRIFT not only has strong discrimination but also uniquely possesses sensitivity to the direction of the recoil nucleus and hence of the WIMP.

Nevertheless, in condensed targets, a variety of detector responses have been found empirically to allow nuclear recoil discrimination. These include using pulse shape in NaI (60), the relative sizes of thermal bolometric signal versus ionization (61, 62), and scintillation versus thermal bolometric signal (63, 64). Discrimination efficiencies greater than 99% for events above a few to a few tens of keV energy deposition are now being reported.

2.5 Backgrounds Common to Different Underground Experiments

Underground experiments vary greatly in the physics questions they pursue, detection techniques they use, materials included in their construction, and processes to which they are sensitive. Yet, despite the wide differences between experiments, all underground experiments are exposed to the same underlying background radiation environment. This environment includes:

1. Direct interactions of particles produced by radioactivity outside the experiment itself (primarily the rock walls), such as ^{40}K gamma rays and (α, n) neutrons from uranium and thorium in the rock.
2. Radioactive impurities incorporated into the detector material or any of the surrounding materials of the experiment. These activities may arise from long-lived isotopes of the specific material itself, from leftover chemical impurities present in the ore or mineral source of the material, or from contamination with substances used in the manufacture of components. Contamination with environmental radioactivities such as radon is also a source of materials background.
3. Radioactivities produced in the "pure" materials of the detector or surroundings by nuclear interactions. Neutron activation by cosmic ray shower neutrons is the dominant process near the Earth's surface. However, photodisintegration by gamma rays and by the effective field of relativistic cosmic ray muons also can contribute, as can nuclear reactions induced by alpha particles.
4. Direct interactions of cosmic ray shower particles in the detector. The interactions of neutrons, muons, and pions dominate near the Earth's surface. At the depth of most underground laboratories, nuclear interactions of cosmic ray muons and neutrinos are all that is left. These particles may interact directly with the detector or indirectly through secondary neutrons and photons from nearby showers in the rock, the shielding, or other non-detector components.

It is important to note that the present discussion of backgrounds underground will present a description of the underground radiation environment and the physical mechanisms producing it, rather than attempting to predict what specific background problems will affect each particular detector or location.

3 UNDERGROUND LABORATORIES

There are fewer than a dozen underground sites worldwide with depths greater than 250 m and active physics research programs. These range from large international facilities with elaborate infrastructure, hundreds of physicist participants, and easy access for large apparatus via road tunnel (LNGS) or truck-sized lifts, to small national facilities housed in working mines with limited infrastructure and access defined by the requirements of mining and the size of vertical mine shaft elevators.

Table 4 lists the operating facilities at the time of this writing, along with a few relevant characteristics for each.

Table 4: Currently operating underground facilities and their characteristics.

Laboratory	Depth (m)	Depth (mwe)	Rock Type	Lab area (m^2)	Access	website
Gran Sasso, Italy	1400	3800	Dedicated, rock	5400	Horizontal	www.lngs.infn.it
Baksan, Russia	Up to 2000	Up to 4800	Dedicated, rock	600	Horizontal	www.inr.ac.ru/INR .../Baksan.html
Canfranc, Spain	Up to 860	Up to 2450	Dedicated, rock	172	Horizontal	www.unizar.es/lfnae .../lfnae_eng.html
Modane (Fréjus), France	1760	4600	Dedicated, rock	410	Horizontal	www-lsm.in2p3.fr
Solotvina, Ukraine	430	1000	Mine (salt)			
WIPP, U.S.	600	1600	Mine (salt; nuclear waste)	Up to 4000	Vertical Truck lift	www.wipp.carlsbad.nm.us .../science/index.htm
Soudan, U.S.	710	2100	Non-op. mine (metals)	Up to 4000	Vertical	www.hep.umn.edu .../soudan
CUPP, Finland	To 980 m	Up to $\sim$ 2700	Mine (metals)	Up to 4000	Vertical and truck ramp	cupp.oulu.fi/site.html
Kamioka, Japan	1000	2700	Mine (metals)	Over 750	Horizontal	www-sk.icrr.u-tokyo.ac.jp
Boulby, U.K.	1100	3000	Mine (salt)	1000	Vertical	hepwww.rl.ac.uk/ukdmc .../boulby/boulby.html
Sudbury, Canada	2160	6000	Mine (metals)	380 + new construction	Vertical	www.sno.phy.queensu.ca www.physics.carleton.ca .../research/snolab

The lab-area figures include space dedicated to single large experiments that are not anticipated to move, such as Super-Kamiokande in Kamioka.

The distinction between metals and salt mines is of interest because salt sites tend to have significantly lower low-energy backgrounds of both neutrons and gamma rays at a given depth (see below). The depth of the facility is equally important in determining the types of physics that can be addressed by an experiment. Figure 2 shows the depth of several underground laboratories, along with the expected vertical cosmic ray flux. SNO is currently the deepest single-purpose laboratory in operation.

Most underground facilities currently house more than one experiment. At the time of this writing, several proposals have been made to either expand existing laboratories (SNOLab)) (67) or erect new ones (DUSEL) (68).

4 DIRECT INTERACTIONS OF HIGH-ENERGY COSMIC RAYS

The study of cosmic radiation is very mature, and authoritative reviews exist (69). The 1000 g/cm^2 thickness of the atmosphere is many times a hadronic interaction length ($\sim$90 g/cm^2). Therefore, energetic cosmic ray primaries (mainly nucleons and nuclei) interact at high altitude, producing well-developed hadronic showers by ground level. At ground level, particles are 75% muons and the remainder are pions, protons, neutrons, electrons, and gamma rays. The arrival times of nearby particles are not statistically independent but rather strongly correlated because such particles probably originate from the same shower.

The energy spectra of the various cosmic ray particle species at sea level are “equilibrated”; passage through more air would not substantially change the energy spectra.

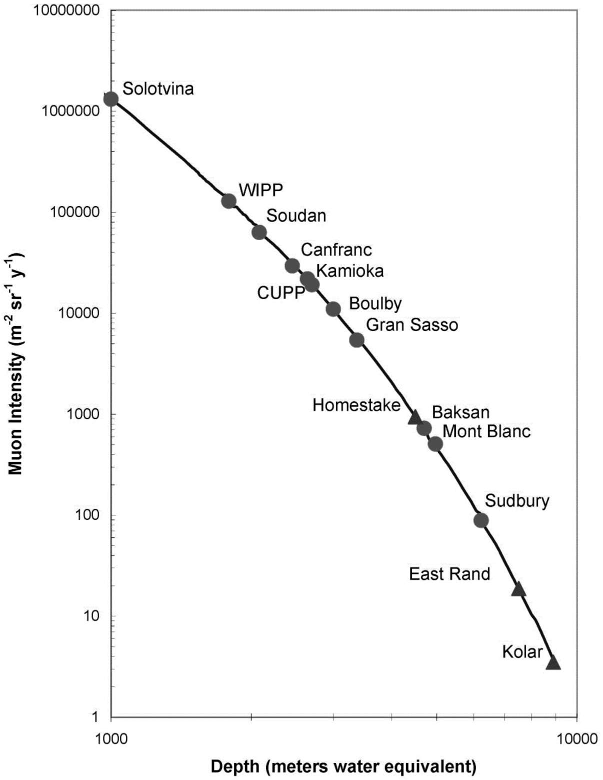

Figure 2: Vertical muon flux as a function of depth, normalized to meter water equivalent (mwe), with current (*circles*) and closed (*triangles*) underground facilities. The CUPP and Kamioka cites are at equal depth.

4.1 Muons

Muons in and of themselves do not usually constitute a serious background to underground experiments, since the muons are easily identified and/or vetoed as they pass through the detector. Muon-induced spallation produces short charged tracks at the event site, possible secondary neutrons, and delayed decays of radioactive products. Unwanted events from the first and last categories can be suppressed greatly by rejection of multiple interactions and of interactions with too great an energy deposition occurring nearby in time and space, and by recoil nucleus discrimination.

However, muon-induced backgrounds are still important in several ways. First, the muon veto rate contributes to the experiment's dead time. This, however, is only important at relatively shallow sites, where muon rates are high. Second, low-energy negative muons can stop and undergo nuclear capture in any material, often giving rise to neutrons and unwanted radioactive isotopes. Such backgrounds are also more important at shallow sites, where the rate of stopping muons is relatively high.

High-energy muons often create spallation products, such as neutrons, photons, and radioisotopes, which can cause serious backgrounds for low-energy experiments. The secondary neutrons produced by high-energy muons interacting in the surrounding rock, in the local shielding, and in the detector itself are not easily tagged. Particularly difficult are the neutrons produced in the adjacent rock, which are not necessarily in time coincidence with a muon veto that covers the entire experiment and its shielding. These neutrons may represent a fundamental limiting background that only deeper sites (68,70) can reduce sufficiently to allow the coming generation of ton-scale experiments to succeed.

The flux of muons underground has been studied for many years. Most recently, measurements of the muon flux as a function of depth have been reported by the Frèjus (71), MACRO (72), and LVD (73) experiments. For muon energies between 10 GeV and 100 TeV, one can use a simple relation to describe the energy and angular dependence of the muon flux at the Earth's surface (77):

$$\frac{dN_\mu}{dE_\mu d\Omega} \simeq 0.14 E_\mu^{-(\gamma-1)} \left(\frac{1}{1+\frac{1.1E_\mu\cos\theta}{115\mathrm{GeV}}} + \frac{0.054}{1+\frac{1.1E_\mu\cos\theta}{850\mathrm{GeV}}}\right)\ \mathrm{cm}^{-2}\mathrm{s}^{-1}\mathrm{sr}^{-1}\mathrm{GeV}^{-1}, \quad (3)$$

where $\gamma - 1 = 2.78 \pm 0.05$. This formula describes the spectral shape with relative

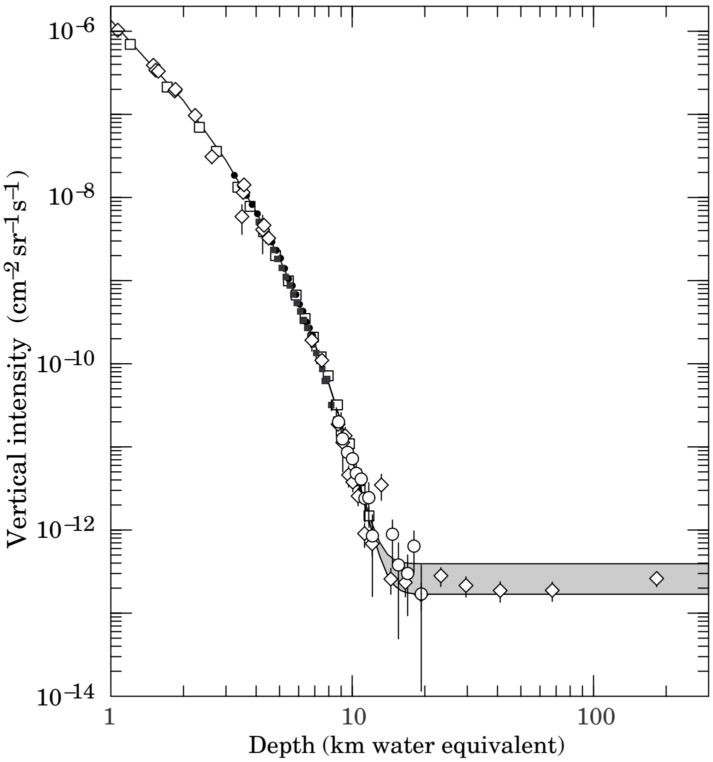

Figure 3: Vertical muon intensity versus depth. The experimental data are from the compilations of Crouch (*diamonds*) (74), Baksan (*open squares*) (75), LVD (*open circles*) (73), MACRO (*filled circles*) (72), and Frèjus (*filled squares*) (71). The shaded area at large depths represents neutrino-induced muons of energy above 2 GeV. The upper line is for horizontal neutrino-induced muons, the lower one for vertically upward muons. From Reference (76) with permission.

errors around 5%. The error on the total flux, however, is much larger, near 20%.

As the muon traverses the rock, it loses energy through ionization, bremsstrahlung, e^+e^- pair production, and photoproduction. The average total rate of energy loss varies linearly with energy according to (77)

$$-\langle\frac{dE(E_\mu)}{dX}\rangle = \alpha + \beta E_\mu \tag{4}$$

The parameters α and β vary logarithmically with energy, whereas their ratio

Table 5: Constants for muon energy loss

Energy (GeV)	α (GeV g^{-1} cm^2)	β (g^{-1} cm^2)	ϵ (GeV)
10.	2.17×10^{-3}	1.90×10^{-6}	1142
100.	2.44×10^{-3}	3.04×10^{-6}	803
1000.	2.68×10^{-3}	3.92×10^{-6}	684
10000.	2.93×10^{-3}	4.35×10^{-6}	674

($\epsilon \equiv \alpha/\beta$) is fairly constant above 10 GeV (see Table 5).

By neglecting fluctuations in the energy loss, Lipari et al. was able to show a simple relation between depth and muon intensity (78).

$$I(X) = I_0 \frac{\epsilon^{1-\gamma}}{\gamma - 1} e^{-(\gamma-1)\beta X}(1 - e^{-\beta X})^{1-\gamma} \approx A(\frac{X_0}{X})^{\eta} e^{-\frac{X}{X_0}} \tag{5}$$

where $X_0 \equiv \beta(\gamma - 1)^{-1}$ and $\eta \equiv \gamma - 1$. Fits to existing data show $A = (2.15 \pm 0.08) \times 10^{-6}$ cm^{-2}s^{-1}sr^{-1}, $\eta = 1.93^{+0.20}_{-0.12}$, and $X_0 = 1155^{+60}_{-30}$ mwe (79).

At large depths, however, fluctuations become large and averages such as Equations 4 and 5 no longer adequately characterize the background situation. Simulation codes such as PROM_MU (80) and MUSIC (81) are well tested against existing data and appear to adequately describe the rare, high-energy physics processes that dominate at large depths. Typical differences in the energy spectrum between the simple Gaisser parameterization using Equation 4 and full simulations are around 5% (11).

4.2 Neutrinos

Neutrinos constitute a signal rather than background for some underground experiments. Nevertheless, experiments that are not specifically designed to measure high-energy neutrinos are susceptible to backgrounds from this source in a number of ways. First, neutrino interactions within the detector (particularly high-energy atmospheric neutrinos) can cause various backgrounds:

$$\bar{\nu}_l + p \to l^+ + n \tag{6}$$

$$\nu_l + n \to l^- + p \tag{7}$$

$$\bar{\nu}_l + N \to \bar{\nu}_l + N. \tag{8}$$

It is possible to characterize the cosmic ray flux of muon neutrinos at the earth's surface (above 10 GeV) in much the same way as the muon flux (82):

$$\frac{d^2\Phi_{\nu\mu}}{d\Omega dE_\nu} \simeq 0.0286 E_\nu^{-2.7} \left(\frac{1}{1 + \frac{6E_\nu \cos(\theta)}{115\ \text{GeV}}} + \frac{0.213}{1 + \frac{1.44E_\nu \cos(\theta)}{850\ \text{GeV}}} \right)\ (\ \text{cm}^{-2}\text{s}^{-1}\text{sr}^{-1}\text{GeV}^{-1}), \tag{9}$$

with a similar expression for electron neutrinos. When folded with the neutrino cross section, one finds the typical interaction rate is on the order of ~ 0.2 events/ton/year (on ^{16}O), dominated mainly by quasielastic nuclear scattering. There is, of course, no way to shield against this background. Such events must be removed from the data by studying event topologies or through explicit calculation and subtraction. A more detailed review of atmospheric neutrinos underground has been done by Gaisser and Honda (83).

Neutrinos also contribute to underground backgrounds through the production of muons via the reaction $\bar{\nu}_\mu + N \to \mu + X$. Because the flux from atmospheric neutrinos is basically isotropic, so are the muons produced from these interactions. Lipari et al. recently has calculated the contribution of neutrino-induced muons (78). Although this is a small fraction of the overall muon rate seen for most underground experiments, it shows that there does exists a lowest depth of ∼ 14 km water equivalents, beyond which the flux is dominated entirely by neutrinos.

Detailed Monte Carlo utilities have recently been developed in order to properly simulate neutrino interactions from atmospheric neutrinos at given depths. Codes such as NUANCE (84), NEUGEN (85), and NUX (86) are structured to simulate all neutrino processes, including quasielastic, resonance, and deep-inelastic scattering. A recent comprehensive analysis of these event generators shows reasonable agreement with neutrino beam data (87).

5 SECONDARY PRODUCTS OF COSMIC RAY INTERACTIONS

5.1 Mechanisms of Neutron Production by Muons

Neutrons are produced underground by muon-induced spallation and by natural radioactivity through (α,n) reactions and spontaneous fission. At depths greater than a few tens of meters, the radioactive processes dominate the total neutron production rate. However, the neutron spectrum from spallation is significantly harder, extending up to several GeV in neutron energy. Furthermore, the high-energy spallation neutron component is in equilibrium with the muon and hadron flux in the rock. Therefore attempting to shield against it will only produce more background at about the same rate as it is removed.

The hard neutron flux in equilibrated showers can be reduced by changing the medium in which the showers propagate. In particle accelerator environments, iron or iron-bearing concrete are favored material for this (88). Iron has a low neuron albedo and large cross sections for inelastic scattering, which rapidly lower the average energy of neutrons in the shower. The water and possibly other neutron capture agents added to the concrete then remove neutrons from the low-energy end of the spectrum. Cost-effective concrete mixtures optimized for neutron removal have been described (89). Detailed simulations for individual underground experiments will be needed to assess the effectiveness of this method.

Cosmic ray muons produce neutrons through several different mechanisms, each of which dominates at different energies and depths. The processes that contribute to this neutron production include the following:

1. Negative muon capture on nuclei.
2. Electromagnetic showers generated by muons.
3. Muon interactions with nuclei via the exchange of virtual photons.
4. Muon-nucleon quasielastic scattering.
5. Secondary neutron production from any of the above processes.

Each of these processes is described in greater detail below.

5.1.1 MUON CAPTURE

Once a negative muon is of sufficiently low energy, it can be attracted into the Coulomb field of a nucleus, forming a "muonic atom" bound state. The bound muon quickly cascades down to the $1s$ state, where it will either decay:

$$\mu^- \rightarrow e^- + \bar{\nu}_e + \nu_\mu, \tag{10}$$

or else undergo nuclear capture via the weak charged-current process:

$$\mu^- + \mathrm{A(Z,N)} \rightarrow \nu_\mu + \mathrm{A(Z-1,N+1)}. \tag{11}$$

The number of neutrons from muon capture can be computed from the following expression:

$$N_n(h) = I_\mu(h) \otimes P_{\mu^-} \otimes P_c \otimes P_n. \tag{12}$$

Here, $N_n(h)$ is the total number of neutrons produced by stopped muons at a depth h, $I_\mu(h)$ is the flux of μ^- stopping at a given depth, P_{μ^-} is the relative charge fraction of cosmic ray muons, P_c is the capture probability, and P_n is the neutron multiplicity following capture.

The muon stopping rate as a function of depth (I_μ), as well as the muon charge fraction (P_{μ^-}), has been studied in detail by Charalambus (91) and Bilokon (92). The principles used to compute the muon stopping function are the same as are needed in general for muon transport through matter, and thus are described by well-known cross sections and fluxes. Uncertainties that dominate the direct interactions in deep sites, such as photonuclear cross sections at high energy, do not significantly affect calculation of the muon energy loss.

Likewise, the μ^-/μ^+ charge ratio has been measured in numerous experiments. The ratio grows logarithmically with muon momentum from 1.2 (at 1 GeV/c) to 1.4 (at 1 TeV/c). Below 1 GeV/c, geomagnetic effects become important and P_{μ^-} therefore varies with position on the Earth (77).

The muon capture probability has also been well studied, both theoretically and experimentally (91, 93, 94), and is described briefly here. It is possible to relate the capture probability P_c to the capture and decay rates:

$$P_c = \frac{\Gamma_c}{\Gamma_c + Q\Gamma_d} \tag{13}$$

where

$$\Gamma_d = \frac{1}{\tau_{\mu^+}}. \tag{14}$$

The symbol Q refers to the Huff factor, which corrects the free muon decay rate for the phase space change due to the muonic atom binding energy.

The muon capture rate Γ_c rises as Z^4_{target}. Comprehensive measurements have been made at TRIUMF for a variety of targets (93), and results for a selected sample of those targets are shown in Table 6. Phenomenological models also exist to estimate the muon capture rate. For low-Z targets, one can use the Primakoff model:

$$\Gamma_c(A, Z) = Z^4_{\text{eff}} X_1 (1 - X_2 \frac{A - Z}{2A}), \tag{15}$$

where Z_{eff} is the effective nuclear charge for a given atom, X_1 represents the capture rate in hydrogen, and X_2 takes into account Pauli suppression for the given nuclear environment. Phenomenological fits to available data from TRIUMF yield $X_1 = 170\ \text{s}^{-1}$ and $X_2 = 3.125$. For heavier elements, Pauli suppression becomes more important and higher-order Pauli corrections are necessary.

Finally, the average muon-capture neutron multiplicity (P_n) has been measured for a variety of elements. Table 6 shows some of those measurements.

The energy spectrum of neutrons emitted by muon capture contains direct and evaporation components, as shown in Equations 16 and 17:

$$\frac{dN_{\text{evap}}}{dE_n} \propto E_n^{5/11} e^{-\frac{E_n}{\theta}}, \tag{16}$$

$$\frac{dN_{\text{direct}}}{dE_n} \propto e^{-\frac{E_n}{T}}, \tag{17}$$

Table 6: Huff factors, average neutron multiplicities P_n, and muon mean lifetimes, for negative muons stopping in various targets (multiplicity data from Reference (95) and mean lifetime from Reference (93))

Material	Z (Z_{eff})	Huff factor	Multiplicity	Mean lifetime (ns)
Al	13 (11.48)	0.993	1.262 ± 0.059	864 ± 2
Si	14 (12.22)	0.992	0.864 ± 0.072	758 ± 2
Ca	20 (16.15)	0.985	0.746 ± 0.032	334 ± 2
Fe	26 (19.59)	0.975	1.125 ± 0.041	206 ± 1
Ag	47 (27.95)	0.925	1.615 ± 0.060	87.0 ± 1.5
I	53 (29.27)	0.910	1.436 ± 0.056	83.4 ± 1.5
Au	79 (33.64)	0.850	1.662 ± 0.044	74.3 ± 1.5
Pb	82 (34.18)	0.844	1.709 ± 0.066	74.8 ± 0.4

where $\frac{dN}{dE_n}$ is the neutron energy spectrum, E_n is the neutron kinetic energy, T is obtained from an exponential fit to the high-energy portion of the neutron spectrum, and θ is the neutron evaporative temperature. The parameters T and θ vary with target atomic number, but typical values are $T \sim 10$ MeV and $\theta \sim 1$ MeV (94).

5.1.2 ELECTROMAGNETIC INTERACTIONS

As a muon passes through matter, real photons and electrons from bremsstrahlung and pair production are released and produce particle showers. Typically the contribution from such processes is small. However, the cross sections grow as $\langle Z^2 \rangle$, and thus become more important for high-Z targets, such as lead. In general, the cross sections associated with electromagnetic showers are very well known. In certain cases, the electromagnetic component of showers produced by cosmic rays were explicitly

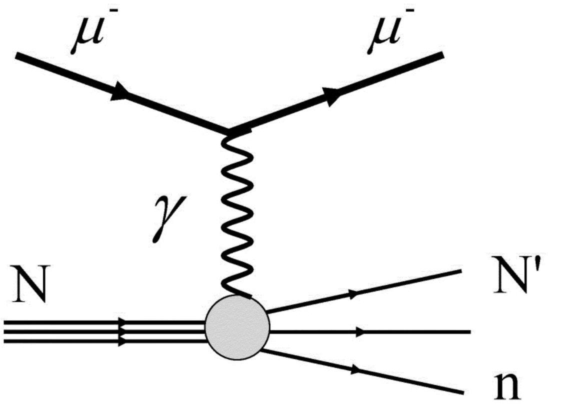

Figure 4: Feynmann diagram showing the virtual photon exchange process in photon-nucleon scattering.

measured and shown to rise linearly with muon energy (96).

5.1.3 Muon Spallation Neutrons produced in muon spallation [2] involve the exchange of a virtual photon as the muon passes through matter (see Figure 4). As it stands, muon spallation via virtual photon exchange is one of the least understood processes in muon interactions at high energies. Theoretically, it is possible to calculate the muon photonuclear cross section by using the equivalent photon approximation. This technique, originally proposed by Fermi (97) and later developed by Weizsäcker (98) and Williams (99), relates the real photonuclear cross section to the virtual cross section by assuming the longitudinal component of the γN cross section (which would apply only to virtual photons) to be negligible:

---

[2] In the literature, this process is also referred to as *muon nuclear interactions* and *photoneutron production.*

$$\sigma_{\mu N} = \int \frac{n_\gamma(\nu)\sigma_{\gamma N}(\nu)}{\nu} d\nu. \tag{18}$$

Here, $n_\gamma(\nu)$ is the virtual photon spectrum associated with the passage of the muon, ν is the photon energy, and $\sigma_{\gamma N}(\nu)$ is the real photon-nucleon cross section.[3] For low energy processes, where the photon interacts with the nucleus collectively, the virtual photon spectrum can be written(101) as a simple energy-dependent expression :

$$n_\gamma(\nu) = \frac{\alpha}{\pi}[\frac{E^2 + E'^2}{p^2} \ln \frac{EE' + PP' - m^2}{m_\mu \nu} - \frac{(E + E')^2}{2P^2} \ln \frac{(P + P')^2}{(E + E')\nu} - \frac{P'}{P}], \tag{19}$$

where E (E') and P (P') are the initial (final) muon energy and momentum, respectively.

Bezrulov and Bugaev $(102, 103)$ have further developed the model of virtual photon exchange within the framework of a generalized vector-meson-dominance model. This model gives a good description of virtual photon exchange in the diffractive region (low 4-momentum transfers and large photon energies). These authors also took into account nuclear shadowing effects that influence muons at high energies. The modified photon spectrum equation is:

$$\begin{aligned} n_\gamma(\omega) &= \frac{\alpha}{2\pi}\omega^2 \Big\{ \frac{1}{4} H(\omega) \ln(1 + \frac{m_2^2}{t}) - \frac{m_\mu^2}{2t}[1 - \frac{m_2^2}{4t} \ln(1 + \frac{m_2^2}{t})] \\ &\quad + 3G(z)[\frac{1}{4} H(\omega)(\ln(1 + \frac{m_1^2}{t}) - \frac{m_1^2}{m_1^2 + t}) - \frac{m_\mu^2}{2t}(1 - \frac{1}{4}\frac{m_1^2}{m_1^2 + t})] \Big\} \end{aligned} \tag{20}$$

Here $\omega \equiv \frac{\nu}{E_\mu}$ and:

$$H(\omega) = \frac{1 + (1 - \omega)^2}{\omega^2}$$

---

[3] For a thorough treatment of the method of equivalent photons, see Reference (100).

$$G(z) = \frac{3}{z}[\frac{1}{2} + \frac{(1+z)e^{-z} - 1}{z^2}]$$

$$z = 0.00282A^{1/3}\sigma_{\gamma p}(\nu)$$

$$t = \frac{m_\mu^2\omega^2}{1-\omega}$$

A is the atomic number of the target, and m_1^2 and m_2^2 are the vector meson masses (with values of 0.51 GeV^2 and 1.80 GeV^2, respectively). Note that the expression is no longer linear in A, but rather has a subtle dependence via the expression $G(z)$, which is due to nuclear shadowing. The trend in the literature has been to use expression 19 for reactions that take place below the pion threshold, while using that of Bezrukov & Bugaev for reactions above it.

Real and virtual photons from the cosmic ray muons produce neutrons through various mechanisms at different energies. in order of increasing energy these include contributions from giant dipole resonance (GDR) absorption quasideuteron photoabsorption (104), $\pi - N$ resonance (105), and deep-inelastic scattering (102, 103). These various components of the σ_{γ_N} cross section are described in more detail in the next section.

5.1.4 PHOTONUCLEAR CROSS-SECTIONS

Because the virtual photon spectrum falls only as $1/E_\mu$ rather than $1/E_\mu^2$, both high-energy and low-energy portions of the γN cross section are important. At low energies (below $\sim$ 30 MeV), photon absorption is dominated by a nuclear collective excitation, the giant dipole resonance (GDR), which decays predominantly by neutron emission. The GDR photo-absorption spectrum is often described by a Lorentian shape:

$$\sigma_{\rm GDR}(E_\gamma) = \Sigma_i A_i \frac{(E_\gamma\Gamma_i)^2}{(E_\gamma - E_i)^2 + (E_\gamma\Gamma_i)^2}, \tag{21}$$

where A_i, E_i, and Γ_i are respectively the empirical peak cross section, energy, and width of the excitation for the nucleus in question. The summation denotes whether one is dealing with spherical (i=1) or deformed (i=2) nuclei. The International Atomic Energy Agency has recently compiled a comprehensive review of photonuclear cross sections from threshold to 140 MeV for a variety of nuclear targets and isotopes (http://www-nds.iaea.org/photonuclear).

Above the GDR peak but below the photopion threshold—that is, for photon energies in the range of $40 \leq E_\gamma \leq 140$ MeV—the dominant mechanism of nuclear photoabsorption is described by the quasideuteron model (104). This model relates the nuclear photoabsorption cross section (σ_{qd}) to that of the free deuteron σ_d:

$$\sigma_{qd} = \frac{L}{A} NZ\sigma_d(E_\gamma)f(E_\gamma), \tag{22}$$

where L is the Levinger parameter, and $f(E_\gamma)$ is a Pauli-blocking function. It is possible to parameterize the free deuteron photodisintegration cross section as follows:

$$\sigma_{\mathrm{d}}(E_\gamma) = 61.2\frac{(E_\gamma - 2.224)^{3/2}}{E_\gamma^3}. \tag{23}$$

The cross section and energy are given in units of mb and MeV, respectively. Chadwick et al. have evaluated the effect of the Pauli suppression term $f(E_\gamma)$ explicitly, and show good agreement with experimental data (106) (Figure 5).

Above photon energies of 140 MeV, pion production—particularly through the Δ isobar resonance—becomes the dominant feature in the photonuclear cross section. The rapid decay of the Δ produces πN or $\pi\pi N$, contributing to the neutron production from muons underground. Also, stopping π^- particles form pionic atoms and undergo nuclear absorption, producing energetic neutron pairs

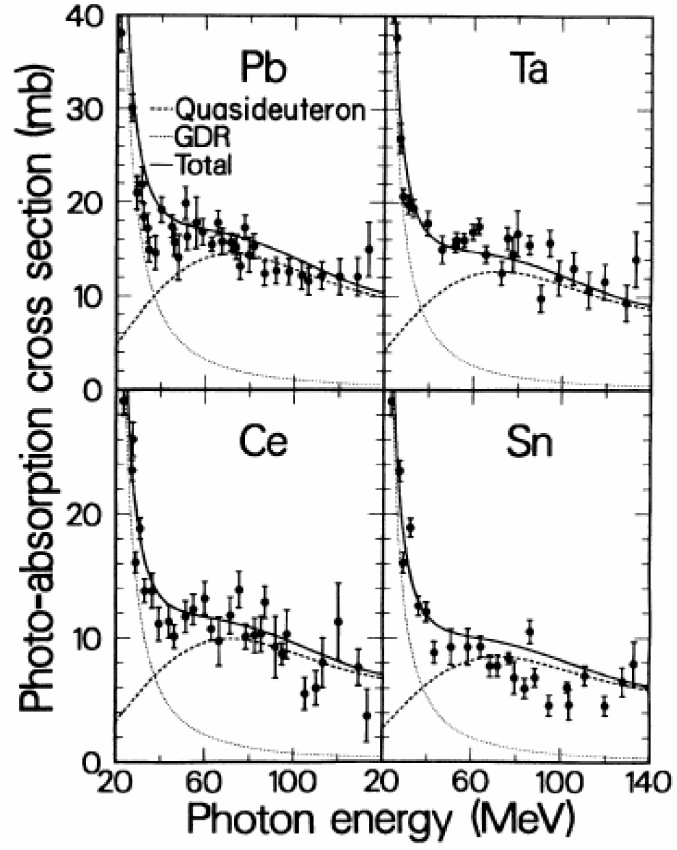

Figure 5: The nuclear photoabsorption cross section as a function of photon energy for Pb, Ta, Sn, and Ce. Curves shows the high energy end of GDR contribution (*dotted line*) and the quasideuteron absorption (*dashed line*). From Reference (106) with permission.

by the ipseudo-deuteron capture mechanism $\pi^- + d \rightarrow n + n$. Even π^+ have a several-percent probability of nuclear absorption as they range out in matter. It has been suggested that correlated double neutron events could serve as a tag for pion production by cosmic muons. Such pairs have been experimentally measured (see Section 6.4). The cross section and contribution of photo-pion production from muons has been explicitly calculated (105), both with and without the equivalent photon approximation, using the cross-section functional forms of Chanfrey et al. (107).

Finally, at photon energies above the Δ resonance, one must consider more general interactions between the photon and the actual participating partons. As mentioned above, Bezrukov & Bugaev (102, 103) have calculated the muon-nucleon cross section within the framework of a vector meson dominance model, taking into account the Q^2 dependence of the meson exchange, as well as nuclear shadowing effects. The original work parametrized the total muon cross section in the form:

$$\sigma_{\gamma N} = 114.3 + 1.647 \ln{(0.0213 E_{\gamma})}^2, \tag{24}$$

with the cross section $\sigma_{\gamma N}$ in μb and the photon energy E_γ in GeV. A more recent treatment of this process (108) used a Regge-type parameterization of the cross section (109):

$$\sigma_{\gamma N} = 67.7 s^{0.0808} + 129 s^{-0.4525}. \tag{25}$$

Here, $s \equiv 2 m_n E_\gamma$ and the energy and cross section again are expressed in GeV and μb, respectively.

Although the bulk of neutron production comes from the high-energy portion of the cross section, the low-energy GDR and quasideuteron components of the muon-nucleon interaction are not negligible ($\sim$ 10–30% of the total neutron rate). Thus, all components must be considered to accurately model neutron/hadron production from cosmic ray muons.

5.1.5 QUASIELASTIC SCATTERING Finally, for completeness, one should also take into account the contribution of neutron production from neutron knockout by muon-nucleus quasielastic scattering. The contribution from this process in the context of underground settings has been computed by DH Perkins (unpublished) using the approximate differential elastic cross section for i muon-neutron scattering:

$$\frac{d\sigma}{dq^2} = \frac{4\pi\alpha^2}{q^4} G_M^2(q^2)\left[\frac{q^2/4M_n^2}{(1+q^2/4M_n^2)} + \left(\frac{q^2}{2M_n^2}\right)\tan\frac{\theta}{2}^2\right], \tag{26}$$

where $G_M(q^2)$ is the neutron magnetic form factor. Because the neutron recoil energy is defined by $T = q^2/2M_n$, the above expression defines both the total cross section and the subsequent neutron recoil spectrum.

6 MONTE-CARLO MODELING OF NEUTRON PRODUCTION UNDERGROUND

6.1 Techniques and Limitations

Even though different components of the muon cross section are both experimentally and theoretically well understood, the prediction of neutron and hadron production underground remains largely uncertain. There are several issues associated with such theoretical estimations. First of all, the Weizsäcker-Williams approach (and its subsequent adaptations) explicitly relies on the premise that the longitudinal polarization state—which exists only for virtual photons—can be ignored. However, at low energies the virtuality of the photon becomes comparable to its energy and thus longitudinal polarization contributions become non-negligible. Second, the low-energy interaction occurs with the nucleus as a whole (giant dipole resonance) rather than individual partons, further complicating the interaction. Finally, the simple factorization of high-energy photoabsorption cross sections into a product of the virtual photon spectrum with the photon-nucleon cross section stems from the relative Q^2-independence of the photon cross section, which is spoiled at higher energies.

However, even if the above issues affecting the primary neutron production processes were negligible or surmountable, the primaries themselves interact further in dense media to produce secondary neutrons, which quickly become dominant at larger depths. Secondary neutron contributions become as large as 75% at high energies or deep sites. Thus, although the theoretical models provide useful guidance for estimating underground backgrounds, their predictive power is still limited without detailed simulation tools.

Recently, several new Monte Carlo models have been developed in order to deal with both the full muon-neutron production cross section and the secondary neutron production. Codes such as FLUKA (110) and GEANT ((111); see also the GEANT4 Web page at CERN, http://geant4.web.cern.ch/geant4) have recently been adopted to simulate high-energy muon interactions taking place in underground experiments. These programs include many different physical processes, including electromagnetic, weak, and nuclear interactions, neutron transport, and so forth. Calculations using these tools are thus better suited than analytical calculations to deal with the problem of particle production from cascade processes. In the next few sections, we examine how such codes compare with existing experimental data.

6.2 Experimental Data on Total Neutron Production Rates Underground

A number of measurements have been carried out to explicitly measure the neutron and hadron production by muons at various depths. Most of the data available are on neutron production, typically involving scintillator targets. A few experiments, however, have also been able to furnish information on neutron spectrum, neutron multiplicity, and pion production.

Several measurements have been made at shallow sites, such as Palo Verde (112), the Stanford Underground Facility (113), and facilities in Russia (102). All have used gadolinium-loaded liquid scintillator as the main target. Gadolinium-loaded scintillator quickly captures neutrons and emits a gamma cascade with a total energy of 8 MeV. As such, the coincidence signature between the entering muon and the subsequent gamma cascade allows the neutron yield from cosmic rays to be measured.

Measurements at deeper sites include those from the Artemovsk Scientific Station (96) (depth 750 wme); the Large Volume Detector (LVD) in Gran Sasso (114) (depth 3650 mwe); and the Large Scintillation Detector (LSD) in Mont Blanc (115) (depth 5200 mwe). Each of these detectors also uses liquid scintillator as the main target. Results from all these experiments are illustrated in Figure 6.

Theoretical models (116) predict that, based on the shower evolution, the neutron production rate should grow as $\sim E_{\mu}^{0.75}$, where E_{μ} is the average muon energy at a given depth. A simple fit to the existing data to the function αE_{μ}^{β} yields $\alpha = (5.12 \pm 0.62) \times 10^{-6}$ and $\beta = 0.73 \pm 0.03$ for scintillator targets. These results can be compared with those predicted from detailed simulations (117):

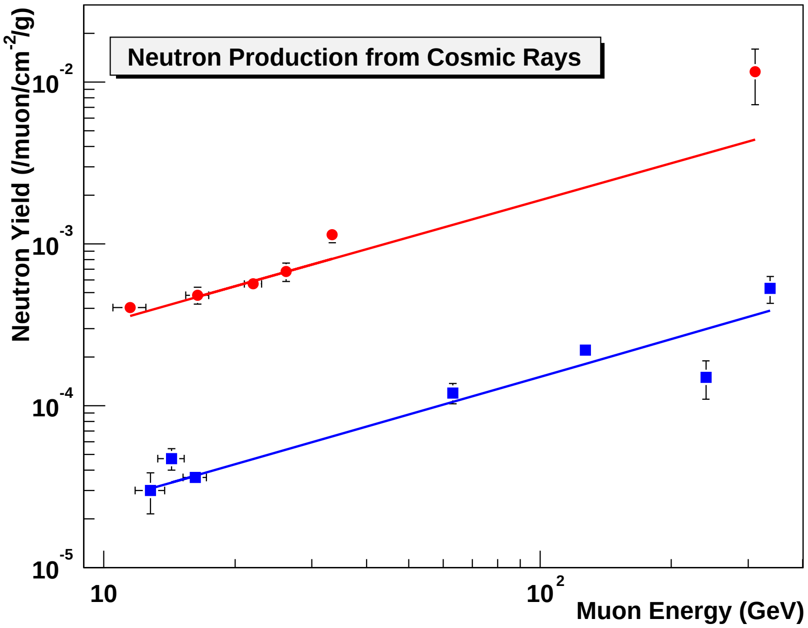

Figure 6: Neutron production rate as a function of average muon energy. Points taken for scintillator (*filled squares*) and lead (*filled circles*) targets at various depths. Solid lines indicate phenomenological fits to the functional form αE_μ^β. See text for details.

$$N_n = 4.14 \times 10^{-6} E_\mu^{0.74} \text{ n}/\mu/\text{g}/\text{cm}^{-2}. \tag{27}$$

Although the energy dependence of muon-induced neutron production is in good agreement with the data, the Monte Carlo predictions tend to underestimate the overall neutron production rate by about 20%.

6.2.1 TARGET DEPENDENCE Although most muon-induced neutron measurements have been made using liquid scintillator, a few earlier measurements also explored neutron production with other targets. Gorshkov & Zyabkin (118–120) measured the neutron production for aluminum, iron, cadmium, and lead at a variety of depths. Similarly, Bergamasco et al. (121) have reported on neutron production from lead targets as deep as 4300 mwe. Figures 6 and 7 summarize these results.

Gorshkov & Bergamasco's data for lead targets at a variety of depths (118–121) gave a combined global fit to the neutron production parameter β for both scintillator and lead data of $\beta = 0.77 \pm 0.03$, again consistent with Monte Carlo and analytical predictions.

The data collected by Gorshkov and colleagues allows further study of the target dependence of neutron production by muons. One can fit the data with the simple relation $\alpha_i \langle A \rangle^{\beta}$, where α_i is allowed to vary for different depths but β is fixed. The best fits are obtained for $\beta = 0.90 \pm 0.23$. One can compare this extracted A-dependence to that predicted by detailed Monte Carlo simulations, where one finds a dependence of $A^{0.76\pm0.01}$ (122, 123). The results are not dissimilar to experimental measurements, though the thickness of the target may prohibit direct comparison.

The target dependence of neutron production from high-energy muons has also recently been studied in the NA55 experiment at the CERN-SPS facility (124). Using a mono-energetic beam of 190 GeV/c^2 muons, the group measured neutron production using thin carbon, copper, and lead targets at different scattering angles. The results of this experiment agree with detailed Monte Carlo simulations to within 15%.

6.3 Total Neutron Energy Spectra

The muon-induced neutron production rate as a function of muon energy is fairly well understood, both experimentally and theoretically. The neutron energy spectrum on the other hand, is still poorly known and descriptions vary widely in the

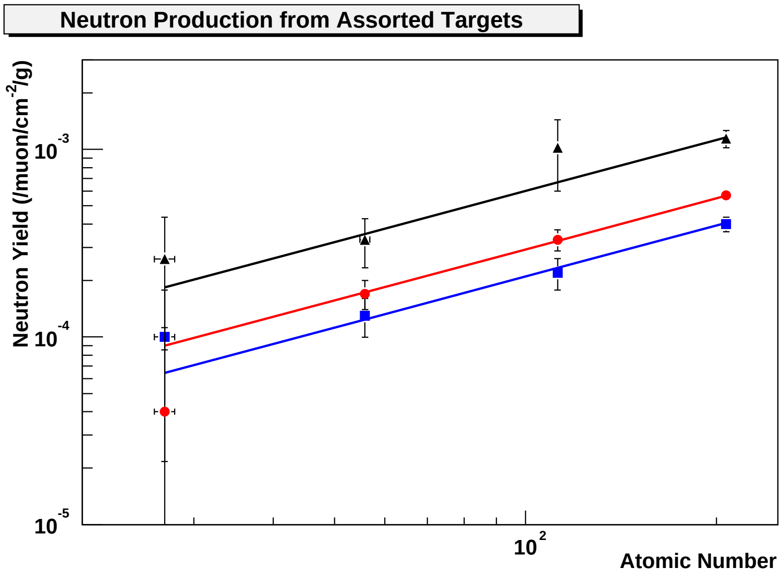

Figure 7: Behavior of neutron production at various depths as a function of atomic weight $\langle A\rangle$ for Al ($\langle A\rangle = 27.0$), Fe ($\langle A\rangle = 55.9$), Cd ($\langle A\rangle = 112.4$), and Pb ($\langle A\rangle = 207.2$). Data taken at 40 mwe (circles), 80 mwe (squares), and 150 mwe (triangles). Lines indicate fit to the function $\alpha_i\langle A\rangle^\beta$, with a best fit of $\beta = 0.90 \pm 0.23$.

literature. Several different parameterizations to fit the observed underground neutron energy spectrum currently exist in the literature. Early work (125) suggests that neutrons of 10–50 MeV have a $T_n^{-1/2}$ dependence (where T_n is the neutron's kinetic energy), while for energies of 50–100 MeV the spectrum becomes flat. At higher energies, analytic calculations by Perkins (unpublished) suggest that in general the spectrum should fall as $T_n^{-1.6}$. According to Khalchukov and others (126), photoneutron measurements taken at accelerator facilities suggest that the spectrum falls more like $T_n^{-1.86}$.

As one can gather from the above, there are conflicting predictions as to how the hard component of the neutron spectrum should evolve. A few experimental measurements are available for comparison against the suggested models, but the measured spectra are not mutually consistent.

The low-energy spectrum of neutrons from high energy muon interactions has been studied using accelerator data from high-energy muon beams (127). Low-energy neutron spectra from muons with up to 490 GeV/c^2 of energy on a lead target can be fit by the expression:

$$\frac{dM}{dT_n} = \frac{M}{\theta^2} e^{-T_n/\theta}, \tag{28}$$

where the empirical parameters are the neutron multiplicity M ,the neutron kinetic energy T_n and the nuclear temperature θ. However, this expression applies only to the neutron spectrum below 10 MeV .

Using the ISIS 800 MeV proton beam to produce muons up to several hundred MeV, the KARMEN collaboration reported a fit to the muon-produced neutron spectrum including both soft and hard components of the following form (128):

$$\frac{dN}{dT_n} = N_{\mathrm{soft}} e^{-T_n/2.1} + N_{\mathrm{hard}} e^{-T_n/39}. \tag{29}$$

Probably the most immediately useful neutron spectral measurements for underground experiments come from the LVD experiment, located at a depth of 3650 mwe (114). At such depths—and thus high muon energies—the high energy neutron spectrum is consistent with a $1/T_n$ dependence.

Both the KARMEN (shallow-site) and the LVD (deep-site) results have recently been compared to Monte Carlo simulations performed with FLUKA (117, 122). The Monte Carlo neutron spectrum was found to be well-represented by the following muon-energy-dependent parametrization:

$$\frac{dN}{dT_n} = A(\frac{e^{-7\ T_n}}{T_n} + B(E_\mu)e^{-2T_n}), \tag{30}$$

where A is the normalization factor and $B(E_\mu)$ is defined as

$$B(E_\mu) = 0.52 - 0.58e^{-0.0099E_\mu}. \tag{31}$$

Figure 8 shows the comparisons between the experimental data and the parametrized Monte Carlo. The simulation describes the measured neutron spectra reasonably well for energies above 20 MeV. What is remarkable about these more recent findings is that FLUKA can describe the spectra at both shallow and deep depths. This confirms the physics model embodied in the program, which ascribes the differences in the observed spectra primarily to the much higher mean muon energy deep underground.

6.4 Pion and Hadron Production

As discussed in the previous section, if the virtual photon energy is above the pion production threshold (around 300 MeV), a Δ resonance can be produced within the nucleus. This reaction is a prominent feature of the photoabsorption cross section. The resonance immediately decays to a πN or $\pi\pi N$ state. Resonance decays produce neutrons both directly in the decay, and also by stopping and nuclear capture of negative pions. The pion capture contribution is enhanced because it usually produces multiple (low energy) neutrons.

The story is different for π^+ production. Positive pions tend not to be captured, but rather to decay:

$$\pi^+ \rightarrow \mu^+\nu_\mu. \tag{32}$$

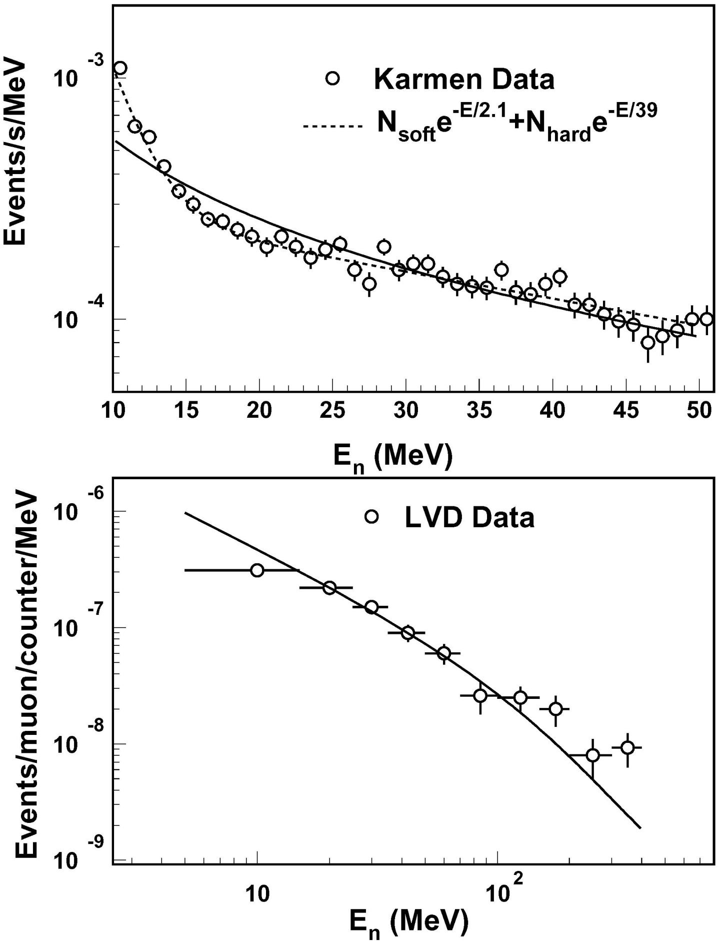

Figure 8: Neutron energy spectrum from the KARMEN and LVD experiments compared to the Monte Carlo predictions from FLUKA, parametrized by Equation 30 from Wang *et al.*. Figure from Reference (117) with permission.

The muon, in turn, will also decay within 2.2 μs of being produced:

$$\mu^+ \rightarrow e^+ \bar{\nu_\mu} \nu_e. \tag{33}$$

This combination of $\pi^+ \rightarrow \mu^+ \rightarrow e^+$ has a distinct timing signature, which has been used in some experiments attempting to tag and measure photonuclear reactions of cosmic rays. Compared with neutrons, positive pions provide a much cleaner tag (both experimentally and theoretically) for measurement of such reactions. Table 7 shows the comparison of π^+ production against analytical (105)

Table 7: Summary of total π^+ yield measurements versus analytical and Monte Carlo predictions

Estimate	Total π^+ Flux ($10^{-6}/\mu/\mathrm{g/cm}^{-2}$
Stanford Underground Facility	3.5 ± 0.2 (stat.) ± 0.7 (sys.)
Analytical calculation	3.0
FLUKA simulation	3.1

Estimate	Muon energy dependence
Data (Reference (96))	$\mathrm{E}_{\mu}^{0.80 \pm 0.20}$
FLUKA	$\mathrm{E}_{\mu}^{0.80}$

and Monte Carlo simulations (117). Although data were taken only at shallow depths, there is generally good agreement between data and predictions.

6.5 Systematic Uncertainties

As the previous sections show, background radiations in underground experiments come from a wide range of sources. Therefore, reliably estimating the uncertainties in predictions is a complex matter. Nevertheless some qualitative arguments with respect to the systematic errors involved for each process can be made. , special attention has been devoted to neutron production from cosmic ray muons thanks to the development of event generators that model the relevant physics. Errors on the overall neutron production are directly correlated with the uncertainties of the muon flux and energy. The muon flux uncertainty, based on underground measurements, is still rather large ($\sim \pm 10\%$) compared with the energy scale uncertainty, which is around ±5%. This implies neutron rate uncertainty of ±10% and ±4%, respectively.

More difficult to characterize are the uncertainties related to the muon-nucleus interactions, for the reasons stated in Section 6.1. At low photon-exchange energies, the equivalent photon approximation begins to break down. At higher energies, uncertainties in the extrapolation of the photon-nucleon cross section play a larger role. For example, a ±1% uncertainty in the muon cross section can translate into a ±15–20% error in flux at large (≥ 20 km) depths for muons.

Similar effects are to be expected for neutrons produced by muons. And, finally, the neutron production from secondary interactions (hadronic showers initiated by the high energy neutrons themselves) becomes dominant at large energies. Secondary nuclear interactions are characterized by large intrinsic fluctuations and by cross-section uncertainties as large as ±20%.

In summary, evaluating the systematics associated with backgrounds underground by analytical or Monte Carlo methods is currently at an early stage. For estimates, direct measurements like those reported by LVD (114), or actual measurements made by the apparatus itself, are probably the most precise way to determine the background rate at a given detector.

7 LOW-ENERGY BACKGROUNDS

7.1 Primordial Radionuclides in Experimental Hardware

Primordial radionuclides are those with such long mean decay lifetimes ($\sim 10^9$ y or more) that they persist in the Earth from the ancient star-stuff that formed the solar system. To achieve the extraordinarily low background levels needed for the present generation of sensitive low-energy experiments underground, primordial radionuclide impurities in the sensitive parts of the experiment must be reduced to the parts-per-trillion range.

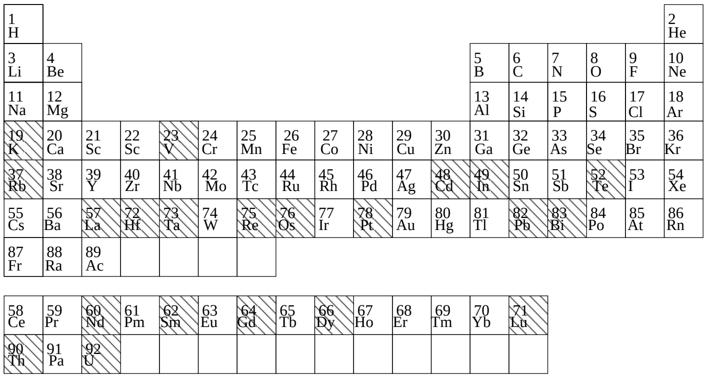

Figure 9: Elements possessing radioisotopes with half-lives exceeding 10^9 y are denoted by hatching.

The distribution throughout the periodic table of the 21 elements having radionuclides with half-lives exceeding 10^9 y is shown in Figure 9. These isotopes occur mainly among the heavier elements. Problem elements include K, Cd, In, Pt, Pb, Bi, and several rare earths. Because of differences in chemical composition of ores, radioisotope abundances of a given chemical element may vary significantly in samples that have different sources and hence different geologic and chemical histories. If chemical elements possessing long-lived isotopes are to be used in low-background apparatus, careful consideration must be given to the effects of the intrinsic radioactivity on the particular experiment.

Primordial radionuclides and their daughters occur in materials for a variety of reasons. The ore or other raw material may have been contaminated while in the ground; the material itself may be made of an element that has one of the very long-lived isotopes in Figure 9; or the material may have been contaminated during manufacturing or synthesis by intentional or unintentional addition of radiocontaminated catalysts, mold releases, lubricants, etc. The levels found in commercial raw materials and manufactured items vary by orders of magnitude. A large online collection of materials' radioactivity data is available from the United Kingdom Dark Matter Collaboration (UKDMC) (http://hepwww.rl.ac.uk/ukdmc/Radioactivity/Index.html).

In practice, the most important primordials observed are ^{40}K and members of the natural ^{238}U and ^{232}Th α decay series.

7.1.1 ^{40}K Potassium is a main source of the background gamma radiation. The lifetime of radioactive isotope ^{40}K is comparable to that of uranium and thorium at 1.277×10^9 y. The decay chain of ^{40}K is far less complex; 89.3% of the time it undergoes a beta decay to the stable state of ^{40}Ca. However, 10.7% of the time the isotope undergoes electron-capture to form ^{40}Ar, and emits a 1460.8 keV photon from the 2^+-to-0^+ transition. The abundance of ^{40}K in natural potassium is 0.0117%, which means that for example ^{nat}KCl has a specific gamma activity of nearly 1.5×10^7 Bq/kg. Potassium normally occurs in rock and concrete as K_2O and K_2CO_3, which are present at the $\sim 1\%$ level. Salt mines, however, may contain veins of KCl, which must be avoided in siting laboratories.

7.1.2 URANIUM AND THORIUM The presence of ^{238}U, ^{235}U, and ^{232}Th often poses a difficult challenge to experiments. These isotopes not only occur widely in the surrounding underground environment but also contribute to a wide variety of background types, mainly high-energy gamma rays, neutrons, and alpha particles. Figures 10 and 11 illustrate the decay chains for ^{238}U and ^{232}Th, respectively. After a series of alpha and beta decays, these decay chains eventually produce the stable lead isotopes ^{206}Pb and ^{208}Pb (130).

High-energy photons are produced by gamma de-excitation in the primordial alpha emitters' decay sequences. Of particular concern are the decays of ^{208}Tl (from the thorium chain) and ^{214}Bi (from the uranium chain). Thirty-six percent

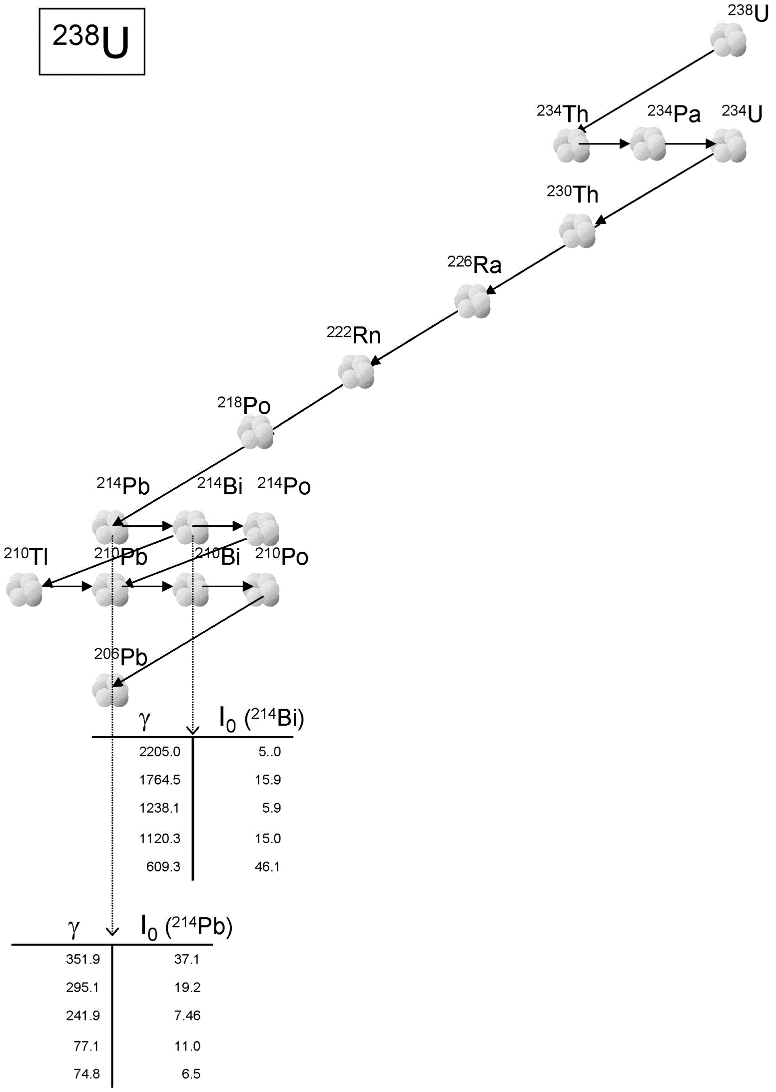

γ	I0 (214Bi)
2205.0	5..0
1764.5	15.9
1238.1	5.9
1120.3	15.0
609.3	46.1

γ	I0 (214Pb)
351.9	37.1
295.1	19.2
241.9	7.46
77.1	11.0
74.8	6.5

Figure 10: The decay sequence from ^{238}U to ^{206}Pb. Right arrow (→) denotes beta decay and slanted downward arrow ($\swarrow$) denotes alpha decay in the chain. The high-intensity ($\geq$ 5%) photons from a given decay are also shown, with energies listed in keV.

of the time, ^{212}Bi alpha-decays to ^{208}Tl, which then emits a 2.614 MeV gamma ray almost 100% of the time. Similarly, ^{214}Pb beta-decays to ^{214}Bi, which emits

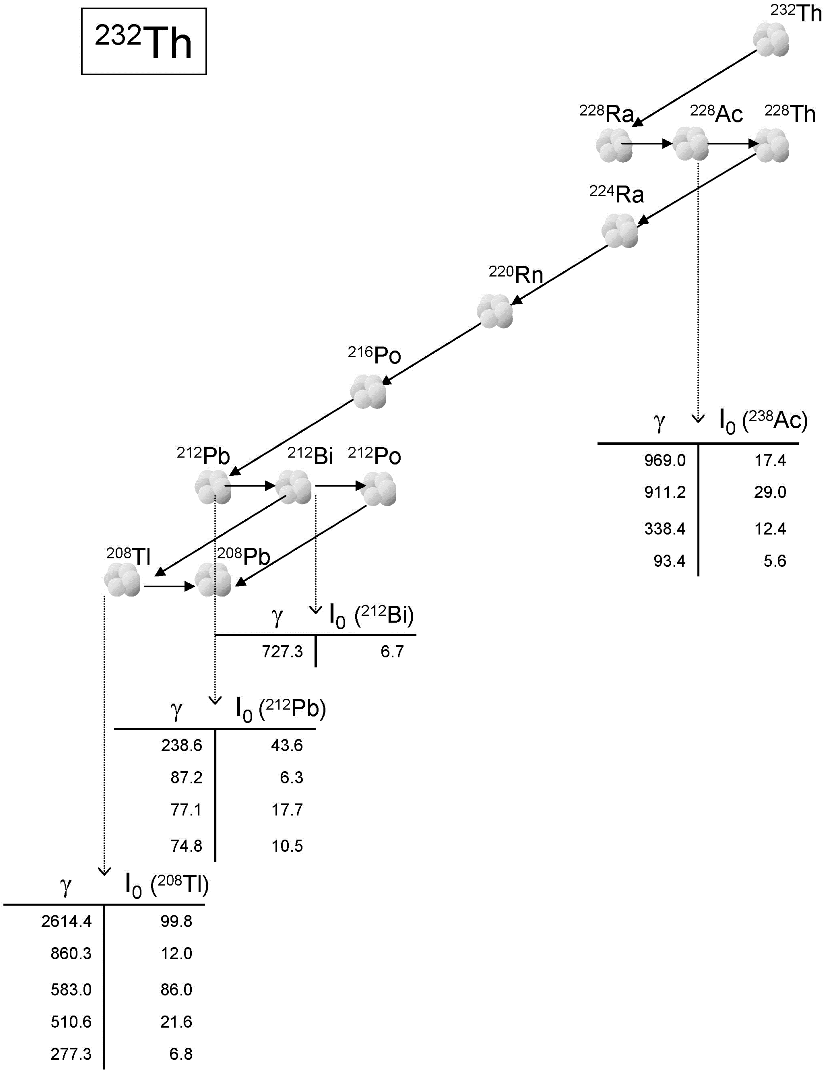

Figure 11: The decay sequence from ^{232}Th to ^{208}Pb. Right arrow (→) denotes beta decay and slanted downward arrow ($\swarrow$) denotes alpha decay in the chain. The high-intensity ($\geq$ 5%) photons from a given decay are also shown, with energies listed in keV.

a 2.204 MeV photon 4.99% of the time and a 2.447 MeV photon 1.55% of the time. Such high-energy photons constitute serious backgrounds for almost all low-energy experiments (dark matter, neutrinoless double beta decay, and solar), unless proper shielding and purification methods are applied.

7.2 Uranium and Thorium Contamination Levels Achieved in Practice

With great care, the content of uranium and thorium in certain specially produced materials have been reduced to the femtogram-per-gram (fg/g) level and lower. The raw materials must be of intrinsically high purity and the manufacturing process must be controlled to exclude intentional or accidental contamination. Examples of this feat include levels near a tenth of a femtogram per gram reported for the BOREXINO liquid scintillator (131).

The Super-Kamiokande experimenters built a water system that purified 50 kton of water to an activity level of 1.4 μBq/m^3, which corresponds to a few tens of femtograms of ^{238}U per gram of water. This was only 3.5 times higher than the levels achieved in the much smaller Kamiokande-III detector. BOREXINO has also purified water for shielding to a similar level (131). The Heidelberg-Moscow group has produced some isotope-separated high-purity ^{76}Ge detectors in which no alpha emission from uranium or thorium was detectable in a 17.7 kg·y exposure (132). Other detectors from the same batch did exhibit a weak but distinct alpha decay peak from the ^{238}U daughter ^{210}Po at an intensity corresponding to less than 100 fg/g. Certain complex industrial materials such as acrylic plastic have also been prepared at very low levels of primordial activity, for example, the 230 fg/g uranium and thorium reported by the SNO group (133). Normal manufactured raw materials tend to be contaminated in the nanograms-per-gram range at best.

7.3 Neutrons from Uranium and Thorium in Rock

At low energies, neutrons from local radioactivity dominate the activation processes and neutron scattering events underground. The intensity of this neutron source is independent of depth underground.

The primordial alpha emitters produce secondary neutrons mainly through (α, n) reactions from the alpha decays in the uranium and thorium chains. For the thorium chain, the important alpha emitters are ^{216}Po (6.8 MeV alpha) and ^{212}Po (8.8 MeV alpha), and for the uranium chain are ^{218}Po (6.0 MeV alpha), ^{214}Po (7.7 MeV alpha), and ^{210}Po (5.3 MeV alpha). Detailed information including tables of (α, n) yields from light nuclides as a function of alpha energy are given by Refs.(134, 135)

Even the most energetic alpha particle (8.8 MeV from the thorium chain) cannot overcome the energy threshold for (α, n) production in ^{16}O, ^{28}Si, and ^{40}Ca. Because these elements constitute more than 75% of the Earth's crust by weight, most of the (α, n) activation comes from the less abundant elements aluminum and sodium, as well as rare isotopes of oxygen, magnesium, and silicon. The reaction is exoergic on naturally occurring ^{9}Be, ^{13}C, ^{17}O, ^{25}Mg, and ^{43}Ca, which are present in hard rock but rare in salt deposits. The (α, n) reaction is also only 1.73 MeV endoergic on ^{29}Si but more than 3.48 MeV endoergic on the stable nuclides of NaCl. Salt mines therefore have a definite advantage over hard rock mines with respect to (α, n), both due to the absence of exoergic reactions on salt nuclides and the generally lower alpha activity (^{238}U) of salt rock.

This is borne out by published measurements of neutron rates in several underground laboratories. At the hard-rock sites Modane (136) and LNGS (143), fast neutron fluxes of 1.6–2.6 $\times 10^{-6}$ n/cm^2/s were reported, while Boulby (123)

Table 8: Spontaneous fission branching ratios and neutron multiplicity for uranium and thorium isotopes

Isotope	B.R. SF/total	Neutron multiplicity
^{238}U	5.45×10^{-7}	1.99 ± 0.03 (139)
^{235}U	7.0×10^{-11}	–
^{232}Th	$< 1.8 \times 10^{-11}$	–

and WIPP(137) salt sites measured only 4×10^{-8} and 4×10^{-7} n/cm^2/s, respectively. The salt sites have much lower neutron fluxes despite their shallower depth.

Direct fission neutrons from uranium and thorium in the rock (particularly ^{238}U) also contribute to the neutron flux (136), but the dominant production mechanism is usually (α, n). This is simply because fission-to-alpha branching ratios for naturally occurring nuclides are very small (see Table 8) (138), usually smaller than the (α, n) probability for alphas stopping in the rock.

Capture of thermal neutrons may also produce secondary radioactivity. On naturally occurring isotopes of Al, Si, Cu, Ge, Xe, Ga, As, and Au, only short-lived activities are produced. Fe, Nb, W, and Hg possess long-lived, neutron-deficient isotopes that can be produced by slow neutron capture.

Low-energy neutrons, below 10 MeV, are strongly attenuated in hydrogenous shielding materials—for example, approximately one decade in intensity per 10 cm of polyethylene (70). For fission neutrons the exponential dose attenuation factor in water(90) is almost 5 (g/cm^2)$^{-1}$.

Feige et al. have used the known (α, n) cross sections coupled with the alpha decay rates of uranium and thorium to calculate the expected neutron production

Table 9: Uranium and thorium concentrations for various types of rocks, along with estimates on neutron production from such sources. Granite types A, B, and C are from rock samples taken in Karkonosze, Poland. Salt types I & II are from Wieliczka Salt Mine, Poland. Tabulation from Reference (141) with permission.

Type of rock	U (ppm)	Th (ppm)	U(α, n)	Th(α, n)	Fission	Total
			(neutrons/g/y)			
Granite	5	11	7.85	7.755	2.33	17.9
Limestone	1	1	0.64	0.285	0.467	1.4
Sandstone	1	1	0.837	0.38	0.467	1.7
Granite A	1.32	7.79	2.24	5.92	0.62	8.8
Granite B	6.25	4.59	10.62	3.49	2.92	17.0
Granite C	1.83	4.38	3.11	3.33	0.85	7.3
Salt I	0.30	2.06	1.60	4.77	0.14	6.5
Salt II	0.13	1.80	4.17	0.69	0.06	4.9

from natural radioactivity for different rock types, according to their composition (140). Florkowski et al. have also computed the expected neutron production from (α, n) and spontaneous fission for various rock species (141). They found neutron production rates from natural radioactivity underground to vary from 2 to 18 neutrons/g/y, depending on the type of rock surrounding the site.

7.4 Neutron Energy Spectra and Direct Measurements

The neutron energy spectrum from natural radioactivity depends on both the specific concentrations of uranium and thorium present in the rock and the exact composition of surrounding geology. In general, however, one can divide the spectrum into two separate components.

The first component is that from the (α, n) reactions from the uranium and thorium chains. If ^{238}U is also present within the structure, one must also include the contribution from spontaneous fission. These neutrons have a soft spectrum with a sharp fall beyond 2 MeV, which can be parameterized by the following equation (142):

$$\frac{dN}{dE_n} = E_n^{1/2} \exp\left(-E_n/1.29\right), \tag{34}$$

where E_n is measured in MeV.

The neutron flux has been explicitly measured at some underground labs, such as Modane (136), Gran Sasso (143–145), Boulby (123), and the Baksan Neutrino Observatory (146). The measured values range from 0.4–4 $\times 10^{-6}$ neutrons/cm^2/s for neutrons above 1 MeV. Analytical estimates by the groups previously mentioned(140, 141) seem to underestimate the total neutron production, but the measurement errors are sufficiently large to accommodate the calculated values. In the case of Gran Sasso, spectral measurements are also available, although different data sets show some disagreement (see Figure 12). It is believed that the differences among results are due to variations in the radon content of the air and the amount of water present in rock formations (129).

7.5 Rock Composition and Geology

Uranium and thorium are responsible for the main low-energy neutron and photon backgrounds in underground sites, so their concentration in materials is of great interest to sensitive experiments. These concentrations vary according to the type of rock present. For example, in granite the typical concentrations of uranium

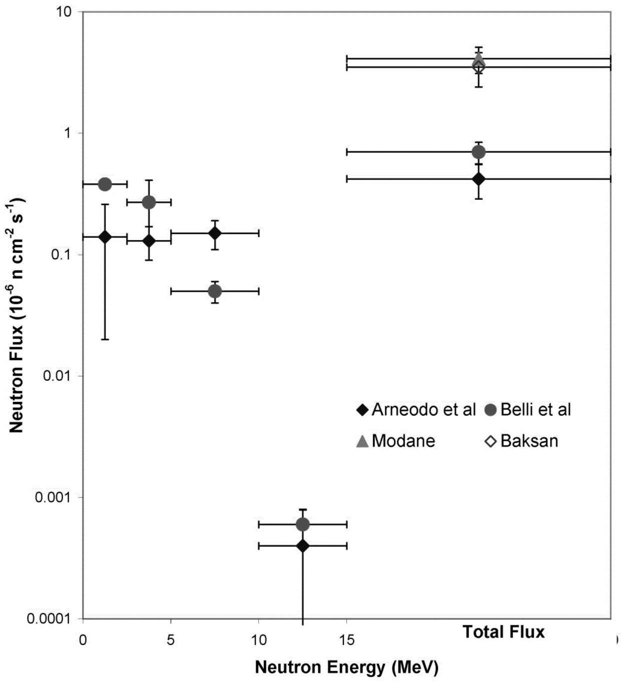

Figure 12: Neutron energy spectrum from rock as measured in Gran Sasso. Data taken from References (144) and (145). Total neutron intensity for Gran Sasso, Modane, and Baksan is shown to the right.

and thorium are 2–6 ppm and 8–33 ppm, respectively. By contrast, basalt-type deposits have very low uranium and thorium concentrations. A brief list of the expected uranium and thorium concentrations in different rock types is provided in Table 10.

7.6 Radon

Radon, a noble gas produced in the decay chains of ^{238}U, ^{235}U, and ^{232}Th, occurs with these primordial radionuclides in rock. As a gas, radon is able to escape both solid and liquid formations. ^{220}Rn, ^{219}Rn, and especially ^{222}Rn are unstable

Table 10: Concentrations of uranium and thorium for various rock types (excerpted from Reference (147))

Rock type	Uranium (ppm)	Thorium (ppm)	Th/U ratio
Granite	2.2–6.1	8–33	3.5–6.3
Gabbros	0.8	3.8	4.3
Basalts	0.1–1	0.2–5	1–5
Ultramafics	< 0.015	< 0.05	variable
Schist	2.5	7.5–19	≥ 3
Phyllite	1.9	5.5	2.9
Slate	2.7	7.5	2.8

isotopes that release several high-energy gammas in the subsequent decay chains. Such a combination of diffusibility and activity makes radon one of the strongest sources of airborne activity above and below the Earth's surface and, as such, it is a limiting factor for most sensitive underground experiments unless appropriate measures are taken to curb its effects.

The most important radon isotope for background considerations is ^{222}Rn. The isotope is produced from the alpha decay of ^{236}Ra, and although its half-life is relatively short ($T_{1/2} = 3.82$ d), it feeds the long-lived (22 y) isotope ^{210}Pb. In addition, subsequent decays of ^{222}Rn feed into several isotopes that emit high-energy photons. Of particular note is the creation of ^{214}Bi, with a 2.447 MeV gamma ray. About 2.3×10^{7} atoms/cm^2/y of ^{222}Rn are released in the atmosphere at the Earth's surface. Levels of 40 Bq/m^3 are common in underground laboratory settings (1). Salt mine sites are often much lower; both Boulby (148) and WIPP report levels below 7 Bq/m^3, consistent with that of outside (surface) air.

This results from a combination of the low uranium and thorium levels in the salt and, in the case of WIPP, very strong ventilation through the site.

Other radon isotopes, such as ^{220}Rn from the thorium decay and ^{219}Rn from the ^{235}U chain, are also active airborne contaminants. However, because their half-lives and those of their daughters are much shorter, they hardly survive the time to diffuse out of the rock matrix. Their activity levels in air are therefore much lower than those of ^{222}Rn.

Diffusion and emanation models can be used to simulate the behavior of radon gas in a given environment. The simplest model describes an isotropic, homogeneous medium in which a nondecaying substance diffuses according to Fick's law (149):

$$\vec{\phi} + D\vec{\nabla}\rho = \mathbf{0}, \tag{35}$$

where D is the diffusion coefficient (cm^2/s), ρ is the local radon concentration (atoms/cm^3), and $\vec{\phi}$ is the radon flux (atoms/cm^2/s). If one invokes the continuity equation,

$$\vec{\nabla}\rho + \partial_{\mathbf{t}}\rho = \mathbf{0}, \tag{36}$$

one then can extract the diffusion equation for radon transport:

$$\partial_t\rho - D\nabla^{\mathbf{2}}\rho = \mathbf{0}. \tag{37}$$

To properly account for the dynamic properties of radon diffusion, the decay constant (λ) and emanation source term ($\mathcal{A}$) must be included:

$$\partial_t\rho - D\nabla^{\mathbf{2}}\rho + \lambda\rho - \mathcal{A} = \mathbf{0}. \tag{38}$$

The complexity of solving these equations depends on the specific geometry of the situation. In general, however, the amount of radon penetrating within the sensitive regions of the detector depends on the diffusion properties and the solubility of radon in the membranes and materials within the system (150).

The solubility of radon in liquids is very high (12.8 cm^3 ^{222}Rn/cm^3 of water and 0.285 cm^3 ^{222}Rn/cm^3 of benzene), so radon is of particular concern to large liquid scintillator or water Cherenkov experiments such as SNO and BOREXINO. However, a number of techniques can be used to reduce the amount of radon present in a detector system. Overpressure of compressed air or evaporated nitrogen from liquid nitrogen reservoirs will help prevent entry of ambient radon into the detector (1). Thorough ventilation of the laboratory with surface air will reduce the ambient concentration as well.

7.7 Other Airborne Activity

Additional radioactivity in the laboratory environment comes from radionuclides present in the atmosphere. These radioactive isotopes, produced mainly by cosmic rays, can be a problem if their activities are large enough. The main isotopes of concern are spallation products from nitrogen and oxygen. Additional radionuclides, such as Others, for example ^{26}Al, ^{36}Cl, and ^{39}Ar, come from cosmic ray interactions with argon. These isotopes are found at much lower concentrations, due to the low relative abundance of argon in the atmosphere. Spallation activities produced from neon, krypton, and xenon are too small to affect most experiments (151).

In addition to activation from cosmic rays, nuclear fallout from weapon testing and power reactors have introduced significant quantities of ^{3}H and ^{14}C, as well as ^{85}Kr, ^{90}Sr, and ^{137}Cs, into the air. In particular, ^{14}C increased almost twofold because of nuclear weapons tests carried out between 1952 and 1962 (152). Such tests have also increased the amount of ^{39}Ar and ^{42}Ar, a key issue for experiments using liquid-argon time-projection-chamber detectors (153, 154). The Chernobyl incident also produced atmospheric releases large enough to be detected in experiments (155). Increases in the production of ^{85}Kr—mostly due to reactors[4]—has also been a issue for low-energy solar neutrino experiments, because ^{85}Kr emits a 3.53 MeV gamma ray (141, 156, 157). Exclusion of atmospheric air is usually practiced to eliminate this route of contamination.

The HDMS experiment provides an example of just how small the concentrations of anthropogenic radionuclides can be made. They reported *no* observable ^{137}Cs activity in 17.7 kg·yr of counting with their isotope-separated ^{76}Ge detectors. This gives an astonishing limit in the neighborhood of 10^{-6} femtogram of ^{137}Cs per gram of Ge. The fission product ^{60}Co was observed in these detectors, but it was probably of cosmogenic origin (see below). In the same experiment, carefully selected and prepared inner copper shielding parts did have measurable ^{137}Cs specific activities, which were 30–100 times larger than the limit for the germanium. This emphasizes how different levels can be, depending on the chemistry of the material in question and its history.

---

[4] ^{85}Kr also can be produced via the spontaneous fission of ^{238}U (cumulative yield is 0.29%) and, thus is naturally found in rock matrices, particularly granite deposits.

Table 11: Atmospheric abundance for selected isotopes. Values for ^{39}Ar and ^{42}Ar are from theoretical calculations including the effects of nuclear weapons testing. Value for ^{85}Kr is from direct measurements made in the Northern Hemisphere in 1985

Isotope	Decay (Max. energy)	Half-life	Activity (Bq/kg)	Flux in Atmospheric (atoms cm^{-2}s^{-1})
^{3}H	β^-(18.6 keV)	12.35 y	0.25	
^{7}Be	E.C. (478 keV)	53.4 d	–	8.1×10^{-3}
^{10}Be	β^- (556 keV)	1.6×10^{6} y	–	0.036
^{14}C	β^- (156 keV)	5730 y	400-500	2.2
^{22}Na	β^+(1275 keV)	2.6 y	–	6×10^{-5}
^{26}Al	β^+(1809 keV)	7.16×10^{6} y	–	1.7×10^{-4}
^{35}S	β^- (167 keV)	7.16×10^{6} y	–	1.4×10^{-3}
^{36}Cl	β^- (709 keV)	3.0×10^{5} y	–	1.1×10^{-3}
^{39}Ar	β^- (565 keV)	269 y	10^{-6}	Negligible
^{42}Ar	β^-(3525 keV from ^{42}K)	32.9 y	$(0.1 - 7.0) \times 10^{-6}$	Negligible
^{85}Kr	β^- (514 keV γ emission)	10.7 y	0.5–0.7	Negligible

8 COSMIC RAYS AND ACTIVATION

8.1 Significance and Composition of Terrestrial Cosmic Rays

The cosmic ray shower particles at the Earth's surface produce inelastic nuclear interactions in rock (Si, O, Ca, C) at a rate of about 2000/kg/d. Only 10% of these interactions are due to the muonic component, the rest to nucleons.(69)

Many of these inelastic interactions produce radioactive nuclei.

At the altitudes of commercial air transportation, the showers are not yet well developed and the rate of inelastic interactions per gram of target material at temperate latitudes is about 200 times greater than at sea level. Aircraft traveling at high geomagnetic latitudes ("polar routes") are subject to rates ten times higher yet for a portion of their flight. Avoiding air transportation of the most sensitive components is often worthwhile (158).

Even very shallow depths below ground (see below) reduce the cosmic ray nucleon rate by many orders of magnitude. The common practice of letting materials exposed at the surface "cool down" underground for several months or even years before use effectively eliminates the short-lived cosmogenic activities.

There are, of course, a number of nuclides with lifetimes too long for this strategy to be effective in a reasonable time (see Figure 13). Spallation products have lower mass number than the target material, often by many mass units. From this fact and the distribution of long-lived nuclides through the periodic table shown in Figure 13 one can see that there are no general rules for selecting materials to eliminate the effects of cosmogenesis. However, light target nuclei do have fewer radioisotopes lying at even lower mass numbers, which can in some cases confer important advantages. An example is the use of highly purified liquid nitrogen as both coolant and shielding material in the proposed GENIUS experiment (159). For the GENUIS germanium detectors themselves, however, no choice of materials is possible and the cosmogenesis problems are severe at the background levels needed in this nondiscriminating experiment. To achieve the required freedom from cosmogenics, the germanium will almost certainly need to be purified and detectors fabricated underground (159). Even experiments with discrimination

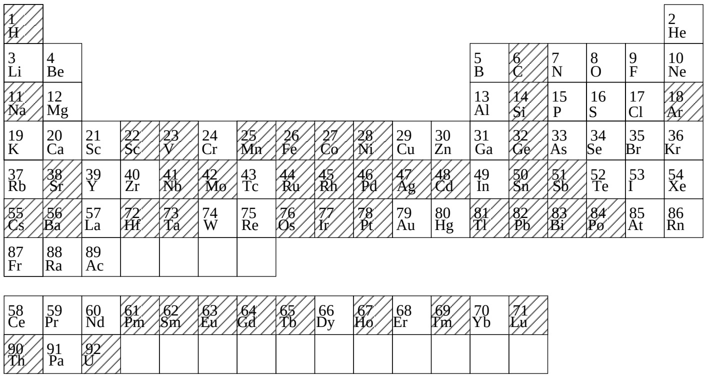

Figure 13: Elements possessing radioisotopes with half-lives between 300 days and 10^4 years are denoted by hatching.

anticipate setting an energy threshold for event candidates above the x-ray backgrounds owing to certain cosmogenics in hyperpure germanium (mainly daughters of germanium isotopes produced by (n, xn)) (70). This is because cross sections for (n, xn) spallation are large, and the detector's discrimination weakens at low energies.

8.2 Spallation in Shallow Underground Sites

At 25 mwe, the muonic "star density" (nuclear interactions per gram of material per unit time) is half its value at the surface, and the nucleonic component is dramatically reduced (fewer than 0.01 inelastic interaction per kilogram per day (69)). The muonic and nucleonic contributions to star density are then about equal, and the total is $\sim$ 100 times less than at the surface. This has allowed such experiments as CDMS I, with very strong discrimination and an external muon veto, to set competitive limits on WIMP dark matter in easily accessible shallow sites (160).

Shallow sites may also be very helpful for avoiding radioactivation of materials during storage or processing. According to calculations using COSMO(166), three months' exposure of initially radiopure Ge at 25 mwe would produce, for example, a few tenths of a Bequerel per kilogram per day of ^{68}Ge, rather than the several tens of counts per day produced by such an exposure at the Earth's surface. Tritium production in germanium (or silicon) would be down to a few hundredths of a Bequerel per kilogram per day per three-month exposure, compared with several Bequerels per kilogram for a similar surface exposure (161).

8.3 Spallation Deep Underground

When an equilibrated cosmic ray shower passes from the air into the solid Earth, an initial spectral re-equilibration occurs within the first few hadronic interaction lengths (few tens of mwe). Following this initial adjustment of the spectra and intensities of shower particles, penetration through more earth simply attenuates the flux of each particle species with a characteristic, nearly energy-independent mean free path.

8.3.1 DIRECT SPALLATION BY MUONS The production of secondary neutrons by muons underground was discussed in Section 5.1. Here we consider the production of radioactive nuclei by the nuclear interactions of cosmic ray muons.

By a depth of 20 m in rock, the inelastic interaction rate of cosmic ray nucleons has fallen six orders of magnitude below that of the muonic component. At greater depths, the direct muonic contribution falls approximately as (69):

$$S(D) = 10^{-7}\text{stars/g sec} \times \left(\frac{D}{30\text{ m}}\right)^{-1.7}. \tag{39}$$

At depths greater than 1500 m in rock, the falloff becomes even steeper. Thus a site 600 m deep (2000 ft in rock), such as WIPP, has a total star density five orders of magnitude lower than that at the surface.

The direct interactions of muons that produce spallation at these depths are mainly quasielastic, deep-inelastic scattering, and photonuclear reactions. Direct muon-induced spallation underground was considered by O'Connell & Schima (162). They predicted an activation rate of

$$N(\text{events/d}) \sim 0.06\phi_\mu N(\text{kton})\sigma_\mu/A, \tag{40}$$

where ϕ_μ is the muon flux per square meter per day, $N(kt)$ is the target mass in kilotons, σ_μ is the muon total inelastic cross section, and A is the target mass number.

These predictions are reasonably consistent with recent experiments in which spallation reactions were tagged by counting muon tracks in coincidence with well-separated neutrons in liquid scintillator (163) and with more direct measurements of delayed beta activity following muon tracks in an underground water-Cherenkov detector (164). A simple rule of thumb based on the deep-inelastic scattering cross section alone is that the mean free path for nuclear interactions by energetic muons is roughly 20 × pc (GeV/c) kilograms per cm^2 with only a weak dependence on target atomic mass. These interactions can be assumed to produce radioactive nuclei with the yield per star coefficients discussed in reference (69). Such order-of-magnitude estimates also compare reasonably well with other direct muon spallation measurements taken with specific targets (^{12}C) conducted at the SPS muon beam at CERN (165).

8.4 Spallation Program COSMO

Martoff has developed and released a computer program, COSMO, to estimate the production of radionuclides in pure materials (166). This program calculates the production of all radionuclides with lifetimes between 25 days and 5 million years, by nucleon-induced spallation of any initial mixture of isotopes. COSMO uses a cosmic ray nucleon spectrum from Reference (69), or one specified by the user. The exposure and postexposure decay times must be defined by the user.

The large yield of ^{3}H in spallation (15% per star) makes it important in the continuum background at a few keV in ultra-low background germanium and silicon detectors (49, 70, 167). Therefore, additional experimental data on tritium production (168) were incorporated into COSMO. The treatment of peripheral reactions was also improved with additional data (169, 170).

Overall accuracy of the cross-section fits underlying COSMO is 20–30%. Actual comparisons between the program predictions and measured cosmogenic activities in detectors often show agreement within a factor of two.

8.5 Case Study: HDMS

The HDMS collaboration has published (171) a detailed analysis of the background in their 17.7 kg·yr counting interval using four isotopically enriched 85% ^{76}Ge detectors. They developed a background model in which source terms were fitted to the observed gamma-ray peaks, with the location of the gamma-ray sources as free parameters. This Monte Carlo–based model fit the continuum well enough to extract a ^{76}Ge $\beta\beta2\nu$ signal with the expected shape. This paper illustrates the practical results of a decade of technical effort aimed at reducing background in this setup to the lowest possible level.

The dominant background below 500 keV was due to 0.36 Bq/kg of 22-year ^{210}Pb in the inner lead shielding. This ^{238}U decay chain daughter was stated to be present alone, i.e., out of secular equilibrium with the rest of the chain. This probably resulted from the high *chemical* purity of the lead used, which left only isotopic impurities at measurable levels. Lines from the complete ^{238}U decay chain were observed, but the background model fits attributed these to the chamber walls, not the lead. The ^{232}Th decay chain was observed at up to 110 μBq/kg in certain copper parts. The second-highest specific activity in the experiment was another primordial, ^{40}K, present in the lead and some copper parts at 100–700 μBq/kg. No primordials were attributed to the detectors themselves, probably because of the extreme chemical purity of the germanium.

Next in order of specific activity were several higher-mass-number, short-lived nuclides that must be anthropogenic. The background model fits placed these on copper internal parts. These nuclides included fission products ^{137}Cs (60–230 μBq/kg; $t_{1/2}$ = 30 y), ^{134}Cs (4–12 μBq/kg; $t_{1/2}$ = 2 y), ^{125}Sb (20–80 μBq/kg; $t_{1/2}$ = 2.7 y). The wide variation in these levels from one copper part of the apparatus to another and the weak correlation of residual activity with half-life show the difficulty of estimating and controlling this type of contamination. ^{207}Bi was also present at 4–20 μBq/kg.

The germanium detectors themselves showed mainly cosmogenic activities with lifetimes near one year;

The germanium detectors themselves showed mainly cosmogenic activities with lifetimes near one year; ^{54}Mn (2.5–4.5 μBq/kg; $t_{1/2}$ = 312 d), ^{57}Co (1.4–3.7 μBq/kg; $t_{1/2}$ = 271 d), ^{65}Zn (6–25 μBq/kg; $t_{1/2}$ = 243 d). ^{58}Co was also attributed to the germanium (0–6 μBq/kg; $t_{1/2}$ = 70 d), which is difficult to understand given the short half-life. The observed ratios of these cosmogenic activities are similar to calculations from the COSMO program (see below), except for the ^{58}Co.

The isotope separation (intended to increase the active mass of $\beta\beta0\nu$-active

^{76}Ge) had the interesting effect of eliminating detectable ^{68}Ge from the detectors. In $^{\mathrm{nat}}$Ge, COSMO predicts that the $(n, 3n)$ reaction produces ^{68}Ge from ^{70}Ge at about 2/3 activity of ^{65}Zn; with isotope-separated ^{76}Ge, a much less probable and more endoergic $(n, 9n)$ reaction is required.

^{70}Ge at about 2/3 activity of ^{65}Zn; with isotope The isotope separation (intended to increase the active mass of $\beta\beta0\nu$-active ^{76}Ge) had the interesting effect of eliminating detectable ^{68}Ge from the detectors. In $^{\mathrm{nat}}$Ge, the $(n, 3n)$ reaction produces ^{68}Ge from ^{70}Ge at about 2/3 activity of ^{65}Zn; with isotope-separated ^{76}Ge, a much less probable and more endoergic $(n, 9n)$ reaction is required.

8.6 Comparison of COSMO Results with Another Experiment

Fisher et al. (155) carried out a $\beta\beta0\nu$ search with $^{\mathrm{nat}}$Ge in a low-activity passive shield of lead and copper. They also fitted their observed backgrounds to measure and localize the radioactivities present, and reported a number of spectra and other details which enable comparison with COSMO predictions. These comparisons are presented here in two tables. Table 12 compares radioactivities quoted by Fisher et. al, both in their Cu shields and their Ge detectors, with those calculated using COSMO. Table 13 shows all the activities predicted by COSMO and indicates whether they were visible at all in the spectra published by Fisher et. al.

Some comments on the agreements and disagreements in these tables follow.

The activity reported for ^{65}Zn in the copper inner shield was 120 counts/(kg·d), considerably higher than the ~5 counts/kg/d calculated for cosmogenic production via ^{65}Cu(p,n)^{65}Zn. There is no explanation evident for this disagreement. A large Zn impurity in the Cu would introduce several (n, xn) channels for ^{65}Zn

Table 12: Comparison of reported activities in copper inner shield and germanium detector from Reference (155) with spallation calculations for activity following three-year exposure and 25-day decay

Nuclide	Half-life (day)	Cu activity counts/(kg·d)	Calculated	Ge activity counts/(kg·d)	Calculated
^{58}Co	70	103	100	121.0	6.1
^{54}Mn	312	45	24	4.1	4.2
^{60}Co	1926	864	23	–	0.9
^{56}Co	78	777	10	4.3	1.2
^{65}Zn	244	121	5.2	–	35.0
^{68}Ge	271	–	–	26.	20.0

production, but this seems unlikely. In comparisons with other experiments, COSMO does not predict anomalously low ^{65}Zn.

The copper also shows comparatively high levels of ^{60,56}Co. These are probably not cosmogenic but may rather be due to airborne fission product contamination from the Chernobyl incident, which occurred at about the time of the experiment. The authors attributed observed ^{134,137}Cs activity to contamination from this source.

No activity for ^{65}Zn in the germanium is quoted. This is puzzling, since according to the calculations it should be the most intense activity present. The 1115 keV photon peak from ^{65}Zn appears broadened in the published spectrum, possibly because of interference from conversion electrons and from the 1120 keV line of cosmogenic ^{46}Sc. The broadening of the ^{65}Zn line may compromise the accuracy with which external and internal activity can be separated using the

Table 13: Activities (> 1 /(kg·d) calculated for cosmic ray spallation of $^{\mathrm{nat}}$Ge for 1095 days, followed by 25 days decay. Results are compared to those of Fisher et al. (155). Nuclides for which the authors gave activities are indicated by "(quoted)" in column 4. Cases in which the activity was not mentioned but where some feature appears to be visible at the expected energy are indicated by "yes." Nuclides where the photon energy is below the 20 keV threshold are indicated by "no."

Isotope	COSMO prediction (counts/(kg·d))	Radiation emitted (keV)	Visible in Ref. (155)?
^{65}Zn	35.0	1115	Yes
^{68}Ge	20.0	511	Yes (26 quoted)
^{73}As	18.0	X-rays only	(no)
^{3}H	6.4	β only	(no)
^{58}Co	6.1	811	Yes (103 quoted)
^{57}Co	4.6	122	Yes
^{54}Mn	4.2	834	Yes (4.1 quoted)
^{55}Fe	2.4	X-rays only	(no)
^{49}V	1.5	X-rays only	(no)
^{51}Cr	1.3	Weak 320	Possibly
^{56}Co	1.2	846,1240,...	Yes (4.3 quoted)

γ ray:γ+X-ray sum peak ratio. This may also partially account for the high reported ^{65}Zn activity of the copper shields.

All the gamma-ray emitters predicted by COSMO are in fact visible in the published spectrum of Reference (155), as indicated in Table 13. Extracting count rates from the raw published spectra has not been attempted, but the smallest visible spectral features represent about one count per kilogram per day.

This section shows that cosmogenic radioactivity can be an important source of background in very low rate experiments deep underground. The COSMO program(166) can provide a useful guide to the expected levels in different materials.

9 CONCLUSIONS

Particle physics underground has amply demonstrated its value by allowing revolutionary discoveries to be made in the physics of solar and atmospheric neutrinos and proton stability. The underground environment is unique because it permits low-background counting experiments. This review has attempted to describe the remaining sources of background that circumscribe the work that can be accomplished underground.

The low-energy and low-rate frontiers can be explored only in the deep underground environment. Experiments that take clever advantage of this environment have been shown capable of extending knowledge beyond the present high-energy frontier, and perhaps beyond any practical extension of it. The next generation of sensitive experiments built on this proven foundation should reveal the secrets of the composition of mass in the universe, the inner workings of the sun, and the ultimate stability of the proton.

Underground laboratories are necessary to carry out underground science. Therefore, the maintenance and establishment of future underground laboratories with even lower backgrounds should be considered a priority for particle physics and astrophysics.

10 Acknowledgments

Joe Formaggio thanks his wife, Jaymi, for her devoted support (both as a partner and as a shrewd editor), and his son, Coby. Jeff Martoff thanks Peter F. Smith and Eugene Loh for their wise counsel and Dan Snowden-Ifft for years of productive collaboration. Both authors also thank Wick Haxton, John Wilkerson, Karsten Heeger, Giorgio Gratta, Don Perkins, Andrew Hime, and Hamish Robertson for their assistance and encouragement in writing this review. This work was supported by the U.S. Department of Energy under Grant No. DE-FG06-90ER40537, the National Science Foundation under Award 0300766, Temple University, and the University of Washington.

11 LITERATURE CITED

Literature Cited

1. Heusser G. *Annu. Rev. Nucl. Part. Sci.* 45:543 (1995)
2. Reines F, et al. *Phys. Rev. Lett.* 15:429 (1965)
3. Achar CV, et al. *Phys. Lett.* 18:196 (1965)
4. Bionta RM, et al. *Phys. Rev. Lett.* 51:27 (1983). Erratum. *Phys. Rev. Lett.* 51:522 (1983)
5. Hirata KS, et al. *Phys. Rev. Lett.* 65:1297 (1990); Hirata KS, et al. *Phys. Rev. D* 44:2241 (1991); Erratum. *Phys. Rev. D* 45:2170 (1992); Fukuda Y, et al. *Phys. Rev. Lett.* 77:1683 (1996)
6. Berger C, et al. *Nucl. Instrum. Methods A* 262:463 (1987)

7. Battistoni G, et al. *Nucl. Instrum. Methods A* 245:277 (1986)
8. De Marzo C, et al. *Nuovo Cim.* C9:281 (1986)
9. Thron JL. *Nucl. Instrum. Methods A* 283:642 (1989)
10. Fukuda S, et al. *Phys. Rev. Lett.* 86:5651 (2001); *Phys. Lett.* B539:179 (2002)
11. Hagiwara K, et al. *Phys. Rev. D* 66:010001 (2002)
12. Fukuda S, et al. *Phys. Rev. Lett.* 81:1562 (1998)
13. Antonioli P. *Nucl. Instrum. Methods A* 433:104 (1999)
14. Jung C K Next Generation Nucleon Decay and Neutrino Detector: Proceedings, Melville, N.Y., American Inst. Phys. (2000)
15. Nakamura K. *Int. J. Mod. Phys.* A18:4053 (2003)
16. Hayato Y, et al. *Phys. Rev. Lett.* 83:1529 (1999)
17. Davis RJ. *Phys. Rev. Lett.* 12:303 (1964)
18. Davis RJ, Harmer DS, Hoffman KC. *Phys. Rev. Lett.* 20:1205 (1968)
19. Cleveland BT, et al. *Astrophys. J.* 496:505 (1998)
20. SAGE Collab. *J. Exp. Theor. Phys.* 95:181 (2002); Abdurashitov JN, et al. *Phys. Rev. C* 60:055801 (1999)
21. Hampel W, et al. *Phys. Lett.* B447:127 (1999)
22. Altmann M, et al. *Phys. Lett.* B490:16 (2000); Kirsten T, *Nucl. Phys. B Proc. Suppl.* 118:33 (2003)
23. Ahmad QR, et al. *Phys. Rev. Lett.* 89:011301 (2002)
24. Ahmad QR, et al. *Phys. Rev. Lett.* 89:011302 (2002)
25. Ahmed SN, et al. *Phys. Rev. Lett.* 92, 181301 (2004)
26. Fogli GL, Lisi E, Marrone A, Palazzo A. *Phys. Lett.* B583:149 (2004)
27. Stonehill LC, et al., *Phys. Rev. C* 69, 015801 (2004)

28. McKinsey DN, Doyle JM. astro-ph/9907314 Horowitz CJ, Coakley KJ, McKinsey DN. *Phys. Rev. D* 68:023005 (2003)
29. Lanou RE, Maris HJ, Seidel GM. *Phys. Rev. Lett.* 58:2498 (1987)
30. Moriyama S. *Presented at the Int. Workshop Technique and Application of Xenon Detectors, Kashiwa, Jpn., Dec. 3–4, 2001*
31. Alimonti G, et al. *Astropart. Phys.* 16:205 (2002)
32. Raghavan RS. *Phys. Rev. Lett.* 78:3618 (1997); Raghavan RS. hep-ex/0106054 (2001)
33. Ejiri H, et al. *Phys. Rev. Lett.* 85:2917 (2000)
34. Bahcall JN, Basu S, Pinsonneault MH. *Phys. Lett.* B433:1 (1998)
35. Bahcall JN, Pena-Garay C. hep-ph/0404061 (2004)
36. der Mateosian E, Goldhaber, M. *Phys. Rev.* 146:810 (1966)
37. Elliott SR, Vogel P. *Annu. Rev. Nucl. Part. Sci.* 52:115 (2002)
38. Moe M, Vogel P. *Annu. Rev. Nucl. Part. Sci.* 44:247 (1994)
39. Danilov M, et al. *Phys. Lett.* B480:12 (2000)
40. Zwicky F, *Helv. Phys. Acta* 6:110 (1933)
41. Trimble V. *Annu. Rev. Astron. Astrophys.* 25:425 (1987)
42. Wagoner RV, Fowler WH, Hoyle F. *Ap. J.* 148:3 (1967)
43. Lee BW, Weinberg S. *Phys. Rev. Lett.* 39:165 (1977)
44. Steigman G, Turner M. *Nucl. Phys. B* 253:375 (1985)
45. Griest K. *Phys. Rev. D* 38:2357 (1988). Erratum. *Phys. Rev. D* 39:3802 (1989)
46. Drukier A, Stodolsky L. *Phys. Rev. D* 30:2295 (1984)
47. Goodman MW, Witten E. *Phys. Rev. D* 31:3059 (1985)
48. Ahlen SP, et al. *Phys. Lett.* B195:603 (1987)

49. Caldwell DO, et al. *Phys. Rev. Lett.* 61:510 (1988)
50. Primack JR, Seckel D, Sadoulet B. *Annu. Rev. Nucl. Part. Sci.* 38:251 (1988)
51. Smith PF, Lewin JD. *Phys. Rep.* 187:203 (1990)
52. Bernabei R, et al. *Nucl. Phys. A* 719:257 (2003)
53. Gaitskell R, Mandic V. http://dmtools.berkeley.edu/limitplots/ (2001)
54. Beck M, et al. *Phys. Lett.* B336:141 (1994)
55. Pröbst F, et al. *Nucl. Phys. B Proc. Suppl.* 110:67 (2002)
56. Klapdor-Kleingrothaus HV, Dietz A, Krivosheina IV. *Nucl. Phys. B Proc. Suppl.* 124:209 (2003)
57. Jochum J, et al. *Nucl. Phys. B Proc. Suppl.* 124:189 (2003)
58. Martoff CJ, et al. *Nucl. Instrum. Methods A* 440:355 (2000)
59. Snowden-Ifft DP, Martoff CJ, Burwell JM. *Phys. Rev. D* 61:101301 (2000)
60. Richardson LW, Wozniak GJ, Maier MR, Moretto LG. *Nucl. Instrum. Methods* 173:485 (1980)
61. Shutt T, et al. *Phys. Rev. Lett.* 69:3425 (1992)
62. Spooner NJC, et al. *Phys. Lett.* B273:333 (1991)
63. Cebrin S, et al. *Nucl. Phys. B Proc. Suppl.* 118:523 (2003)
64. Meunier P, et al. Appl. Phys. Lett. 75:1335 (1999)
65. Mio N. *Prog. Theor. Phys. Suppl.* 151:221 (2003)
66. Broggini C. *Nucl. Phys. Proc. Suppl.* 43:58 (1995)
67. Carleton University, Laurentian University, Queen's University, Université de Montréal, University of British Columbia, University of Guelph, *An International Facility for Underground Science: Proposal to the Canada Fund for Innovation* www.physics.carleton.ca/hotnews/CFI_FINAL.pdfa (2002)

68. Balantekin B (Homestake Collab.) *The national underground science and engineering laboratory at Homestake: project book, reference design stage.* http:int.phys.washington.edu/NUSEL/reference_book.html (2003)
69. Lal D, Peters B. Handbuch der Physik Band 46/2, p. 551-612. ibid, Schopper, I. (1967)
70. Schnee RW, Akerib DS, Gaitskell RJ. *Nuc. Phys. B Proc. Suppl.* 124:233 (2003)
71. Berger C, et al. *Phys. Rev. D* 40:2163 (1989)
72. Ambrosio M, et al. *Phys. Rev. D* 52:3793 (1995)
73. Aglietta M, et al. *Astropart. Phys.* 3:311 (1995)
74. Crouch M. *Proc. Int. Cosmic Ray Conf., 20th, Moscow* 6:165 (1987)
75. Andreev Yu M, Gurentzov VI, Kogai IM. *Proc. Int. Cosmic Ray Conf., 26th, Moscow* 6:200 (1987)
76. Hagiwara K, et al. *Phys. Rev. D* 66:010001 (2002)
77. Gaisser TK. *Cosmic Rays and Particle Physics*. Cambridge Univ. Press, UK (1990)
78. Lipari P, Stanev T. *Phys. Rev. D* 44:3543 (1991)
79. Learned JG, Mannheim K. *Annu. Rev. Nucl. Part. Sci.* 50:679 (2000)
80. Lipari P. *Astropart. Phys.* 1:195 (1993)
81. Antonioli P, et al. *Astropart. Phys.* 7:357 (1997)
82. Volkova LV. *Fiz Y.* 31:1531 (1980); *Sov. J. Nucl. Phys.* 31:784 (1980)
83. Gaisser TK, Honda M. *Annu. Rev. Nucl. Part. Sci.* 52:153 (2002)
84. Casper D. *Nucl. Phys. Proc. Suppl.* 112:161 (2002)
85. Gallagher H. *Nucl. Phys. Proc. Suppl.* 112:188 (2002)
86. Rubbia A. Presented at NuInt01, 1st Int. Workshop Neutrino-Nucleus In-

teract. in Few GeV Region. http://neutrino.kek.jp/nuint01/ (1982)

87. Zeller GP. hep-ex/0312061 (2003)
88. Kaplan MF. *Concrete Radiation Shielding.* New York: Wiley (1989)
89. Finkelstein KD, Gray SW. *Cornell High Energy Synchrotron Source (CHESS) newsletter* (1995)
90. Bostain DA, Brenizer JS, and Norris PM Res. Nondestr. Eval. **14**, 47 (2002)
91. Charalambus S. *Nucl. Phys. A* 166:145 (1971)
92. Biloken H, et al. *J. Geophys. Res.* 94:12,145 (1989)
93. Suzuki T, et al. *Phys. Rev. C* 35:2212 (1987)
94. Measday DF. *Phys. Rep.* 352:243 (2001)
95. MacDonald B, Diaz JA, Kaplan SN, Pyle RV. *Phys. Rev. B* 139:1253 (1965)
96. Enikeev RI, et al. *Sov. J. Nucl. Phys.* 46:1492 (1987)
97. Fermi E. *Physik Z.* 29:315 (1924)
98. Weizsäcker CF. *Z. Phys.* 88:612 (1934)
99. Williams EJ, et al. *Kgl. Dan. Vidensk. Selsk. Mat. Fys. Medd.* XIII:4 (1935)
100. Landau LD, Lifshitz EM. *Course of Theoretical Physics*, Vol. 4, Pt. 1. *Relativistic Quantum Theory*, p. 351., Oxford Pergamon (1971)
101. Dalitz RH, Yennie DR. *Phys. Rev.* 105:1598 (1957)
102. Bezrukov LB, et al. *Sov. J. Nucl. Phys.* 17:51 (1973)
103. Bezrukov LB, Bugaev EV. *Sov. J. Nucl. Phys.* 33:635 (1981)
104. Levinger JS. *Phys. Rev.* 84:43 (1951)
105. Delorme J, Ericson M, Ericson T, Vogel P. *Phys. Rev. C* 52:2222 (1995)
106. Chadwick MB, Oblozinsky P, Hodgson PE, Reffo G. *Phys. Rev. C* 44:814 (1991)
107. Chanfray G, Delorome J, Ericson M, Molinari A. *Nucl. Phys. A* 556:439

(1993)

108. Bugaev EV, et al. *Phys. Rev.* 58:05401 (1998)
109. Donnachie A, Landshoff PV. *Phys. Lett.* B296:227 (1992)
110. Fasso A, Ferrari A, Sala PR. *Proc. Monte Carlo 2000 Conf.*, Lisbon, Spain (2000)
111. Agostinelli S, et al. *Nucl. Instrum. Methods A* 498:250 (2003)
112. Boehm F, et al. *Phys. Rev. D* 62:092005 (2000)
113. Hertenberger R, Chen M, Dougherty BL. *Phys. Rev. C* 52:3449 (1995)
114. Aglietta M, et al. *Proc. Int. Cosmic Ray Conf., 26th*, 2:44 (1999)
115. Aglietta M, et al. *Nuovo Cim.* C12:467 (1989)
116. Ryazhskaya OG, Zatsepin GT. *Proc. Int. Conf. Cosmic Rays, IX*, 3:987. London: Institute of Physics and the Physical Society (1966)
117. Wang YF, et al. *Phys. Rev. D* 64:013012 (2001)
118. Gorshkov GV, Zyabkin VA. *Sov. J. Nucl. Phys.* 7:470 (1968); *Yad. Fiz.* 7:770 (1967)
119. Gorshkov GV, Zyabkin VA. *Sov. J. Nucl. Phys.* 12:187 (1971); *Yad. Fiz.* 12:340 (1970)
120. Gorshkov GV, Zyabkin VA, Yakovlev RM. *Sov. J. Nucl. Phys.* 13:450 (1971); *Yad. Fiz.* 13:791 (1970)
121. Bergamasco L, Costa S, Picchi P. *Nuovo Cim.* A13:403 (1973)
122. Kudryavtsev VA, Spooner NJ, McMillan JE. hep-ex/0303007 (2003)
123. Kudryavtsev VA, et al. hep-ex/0301038 (2003)
124. Chazal V, et al. *Nucl. Phys. A* 663:885 (2000)
125. Barton JC. Proc. Int. Conf. Cosmic Rays, 19th, La Jolla, 1985, p. 98. London: Institute of Physics (1985)

126. Khalchukov FF, et al. *Nuovo Cim.* C6:320 (1983)

127. Adams TR, et al. *Phys. Rev. Lett.* 74:5198 (1995). Errata. *Phys. Rev. Lett.* 80:2020 (1998)

128. Wolf J. *The Indentification of Dark Matter: Proceedings*, Edited by Neil J.C. Spooner and Vitaly Kudryavtsev. River Edge, N.J., World Scientific (2003)

129. Wulandari H. Presented at Int. Workshop Identification of Dark Matter, 4th, York UK (2002)

130. Firestone RB. *Table of Isotopes.* NY Wiley. 8th ed. (1996)

131. Back HO, et al. *Phys. Lett.* B563:23 (2003)

132. Baudis L, et al. *Phys. Rep.* 307:291 (1998)

133. Jagam P, Simpson JJ. *Nucl. Instrum. Methods A* 324:389 (1993)

134. Heaton R, *Nucl. Instrum. Methods A* 276:529 (1989)

135. Heaton R, *Nucl. Geophys.* 4:499 (1990)

136. Chazal V, et al. *Astropart. Phys.* 9:163 (1998)

137. Balbes MJ et al. *Nucl. Instrum. Methods A* 399:269 (1997)

138. Vandenbosch R, Huizenga JR. *Nuclear Fission.* New York: Academic (1973)

139. Popeko AG, et al. *Yad. Fiz.* 24:473 (1975); *Sov. J. Nucl. Phys.* 24:245 (1976)

140. Feige Y, Oltman BG, Kastner J. *J. Geophys. Res.* 73:3135 (1968)

141. Florkowski T, Morawaska L, Rozanski K. *Nucl. Geophys.* 2:1 (1998)

142. Segrè E. *Nuclei and Particles*. Reading, Massachussetts Benjamin & Cummins. 2nd ed. (1977)

143. Rindi A, Celani F, Lindozzi M, Miozzi S. *Nucl. Instrum. Methods A* 272:871

(1988)

144. Belli P, et al. *Nuovo Cim.* A101:959 (1989)
145. Arneodo F, et al. *Nuovo Cim.* A112:819 (1999)
146. Abdurashitov JN, et al. physics/0001007 (2000)
147. Ivanovich M, Harmon RS. *Uranium-series Disequilibrium: Applications to Earth, Marine, and Environmental Sciences.* Oxford, UK: Clarendon (1992)
148. Roberts J. Unpublished communication to Particle and Nuclear Astrophysics and Gravitation International Committee (PANAGIC); quoted at http://www.lngs.infn.it/site/exppro/panagic/sections/particle/experiments/boulby.html
149. Fick A. Ann. Physik, Leipzig 170, 59, (1855)
150. Cadonati L. *The Borexino solar neutrino experiment and its scintillator containment vessel.* PhD thesis, Princeton Univ. (2001)
151. DaSilva AJ. *Development of a low background environment for the cryogenic dark matter search.* PhD thesis, Univ. British Columbia (1996)
152. Choppin GR, Rydberg J. *Nuclear Chemistry.* Oxford UK Pergamon (1980)
153. Barabash AS, Kornoukhov VN, Jants VE. *Nucl. Instrum. Methods A* 385:530 (1997)
154. Cennini P, et al. *Nucl. Instrum. Methods A* 356:526 (1995)
155. Fisher P, et al. *Phys. Lett.* B218:257 (1989)
156. Weiss W, et al. *Nucl. Instrum. Methods B* 17:571 (1986)
157. Currie LA. *IEEE Trans. Nucl. Sci.* NS-19:119 (1972)
158. Baudis L, et al. *Phys. Rev. D* 63:022001 (2000)
159. Klapdor-Kleingrothaus HV, Baudis L, Heusser G, Majorovits B, Päs H. hep-ex/9910205 (1999)

160. Akerib DS, et al. *Phys. Rev. D* 68: 82002 (2003)

161. Martoff CJ. *Science* 237:507 (1987)

162. O'Connell JS, Schima FJ. *Phys. Rev. D* 38:2277 (1988)

163. Aglietta M, et al. *Phys. At. Nuclei* 66:123 (2002)

164. Hirata KS, et al. *Phys. Rev. D* 38:448 (1988)

165. Hagner T, et al. *Astropart. Phys.* 14:33 (2000)

166. Martoff CJ, Lewin D. *Comput. Phys. Commun.* 72:96 (1992)

167. Caldwell DO, et al. *Phys. Rev. Lett.* 65:1305 (1990)

168. Currie LA. *Phys. Rev.* 114:878 (1959)

169. Silberberg R, Tsao C. *Astrophys. J. Suppl.* Ser. 220(I):315; 220(II):335 (1973)

170. Church LB, Caretto AA. *Phys. Rev.* 178:1732 (1969)

171. Günther M, et al. *Phys. Rev. D* 55:54 (1997)